Developments in the CSU-RAMS Aerosol Model: Emissions, Nucleation, Regeneration, Deposition, and Radiation

STEPHEN M. SALEEBY AND SUSAN C. VAN DEN HEEVER

Colorado State University, Fort Collins, Colorado

(Manuscript received 20 November 2012, in final form 22 July 2013)

ABSTRACT

The Colorado State University (CSU) Regional Atmospheric Modeling System (RAMS) has undergone development focused on improving the treatment of aerosols in the microphysics model, with the goal of examining the impacts of aerosol characteristics, scavenging, and regeneration processes, among others, on precipitation processes in clouds ranging from stratocumulus to deep convection and mixed-phase orographic clouds. Improvements in the representation of aerosols allow for more comprehensive studies of aerosol effects on cloud systems across scales. In RAMS there are now sub- and supermicrometer modes of sulfate, mineral dust, sea salt, and regenerated aerosol. All aerosol species can compete for cloud droplet nucleation, and they are regenerated via hydrometeor evaporation. A newly applied heterogeneous ice nuclei parameterization accounts for deposition nucleation and condensation and immersion freezing of aerosols greater than 0.5-μm diameter. There are also schemes for trimodal sea salt emissions and bimodal dust lofting that are functions of wind speed and surface properties. Aerosol wet and dry deposition accounts for collection by falling hydrometeors as well as gravitational settling of aerosols on water, soil, and vegetation. Aerosol radiative effects are parameterized via the Mie theory. An examination of the simulated impact of aerosol characteristics, sources, and sinks reveals mixed sensitivity among cloud types. For example, reduced aerosol solubility has little impact on deep convection since supersaturations are large and nearly all accumulation-mode aerosols activate. In contrast, reduced solubility results in reduced aerosol activation in precipitating stratocumulus. This leads to lower cloud droplet concentration, larger droplet size, and more efficient warm rain processes.

1. Introduction

Accurately simulating aerosol and cloud microphysical processes is becoming increasingly important in process-scale, mesoscale, and climate-scale models. Much of our understanding of aerosol and microphysical effects on the water cycle and global climate rely on the use of such models (Solomon et al. 2007). The indirect effects of cloud and ice nucleating aerosols (Twomey 1974; Albrecht 1989), including cloud albedo, cloud lifetime, and precipitation efficiency, remain relatively poorly understood (Solomon et al. 2007). As such, improvements in the representation of aerosols and related cloud processes in models is necessary to improve confidence regarding aerosol impacts on climate. One such model being used for aerosol and microphysical research across multiple cloud scales is the Colorado State University (CSU) Regional Atmospheric Modeling System (RAMS), version 6.0 (Cotton et al. 2003).

The RAMS model has proven to be versatile across atmospheric scales as a large-eddy-simulation model (e.g., Jiang et al. 2001; Jiang and Feingold 2006), cloud-resolving model (e.g., Saleeby et al. 2009; van den Heever et al. 2006), and regional climate model (e.g., Lu and Shuttleworth 2002; Castro et al. 2007). It has demonstrated success in simulating a range of atmospheric phenomena, such as supercell thunderstorms (e.g., van den Heever and Cotton 2004), mesoscale convective systems (e.g., Olsson and Cotton 1997; Bernardet and Cotton 1998), mixed-phase orographic precipitation (Saleeby et al. 2009, 2011, 2013), monsoon systems (e.g., Saleeby and Cotton 2004b), sea breeze circulations (e.g., Darby et al. 2002), extratropical cyclones (e.g., Igel et al. 2013), and hurricanes (e.g., Zhang et al. 2007; Carrio and Cotton 2011).

RAMS incorporates a two-moment bulk microphysics package that predicts the mixing ratio and number concentration of cloud droplets, drizzle, rain, pristine ice,

Corresponding author address: Stephen M. Saleeby, Colorado State University, Atmospheric Science Department, 1371 Campus Delivery, Fort Collins, CO 80523.
E-mail: smsaleeb@atmos.colostate.edu

DOI: 10.1175/JAMC-D-12-0312.1

snow, aggregates, graupel, and hail (Walko et al. 1995; Meyers et al. 1997; Saleeby and Cotton 2004a). Each hydrometeor species is represented by a gamma distribution, given as

$$N(D) = \frac{N_t}{\Gamma(v)}\left(\frac{D}{D_n}\right)^{v-1}\frac{1}{D_n}\exp\left(-\frac{D}{D_n}\right). \quad (1)$$

(All variables and symbols in this paper are defined in Table 1.) The model microphysics simulates cloud nucleation, ice nucleation, vapor deposition, evaporation, collision–coalescence, melting, freezing, sedimentation, and secondary ice production (Verlinde et al. 1990; DeMott et al. 1994; Walko et al. 1995, 2000a; Meyers et al. 1992, 1997; Cotton et al. 2003; Saleeby and Cotton 2004a, 2008). The two-stream radiation model of Harrington (1997) accounts for attenuation and scattering of hydrometeors.

Saleeby and Cotton (2004a) implemented a cloud nucleation scheme in RAMS, version 4.3, for two-moment prediction of cloud and drizzle droplets. Lagrangian parcel-bin simulations were performed offline with a single-column model (Heymsfield and Sabin 1989; Feingold and Heymsfield 1992) to generate lookup tables that contain the percentage of aerosols that activate over a range of vertical velocity, temperature, aerosol concentration, and aerosol size. Studies using this aerosol parameterization have examined the cloud droplet nucleating effects of aerosols over a wide variety of cloud systems, including orographic snowfall (Saleeby et al. 2009, 2011, 2013), shallow clouds (Cheng et al. 2009; Lee et al. 2009), deep convection (Lee 2012; van den Heever et al. 2006, 2011; Storer and van den Heever 2013), hurricanes (Zhang et al. 2007; Carrio and Cotton 2011), and extratropical cyclones (Igel et al. 2013). Stokowski (2005) expanded the model capability by implementing an aerosol–radiation interaction scheme, and he presented an investigation of noncloudy aerosol layer radiative effects. Smith (2007) and Seigel and van den Heever (2012) discuss the development of a mineral dust source model and removal by dry and wet deposition for investigating dust transport in various systems. Carrio and Cotton (2011) discuss an implemented sea salt source model and a wet scavenging scheme for use in examining the impact of sea salt on tropical cyclones. While much has been learned about aerosol effects from these studies above, the RAMS aerosol modules used in these past studies lacked one or more of the following areas of aerosol representation: multiple aerosol modes, variable solubility, nucleation scavenging, regeneration, scavenging by dry and wet deposition, aerosol–radiation interactions, and/or the ability to track the temporal and spatial variability in activated, scavenged, and in situ aerosols by type. As such, even more could potentially have been gained from a more comprehensive treatment of aerosols.

With use of a cloud parcel model, Flossmann et al. (1985, 1987) demonstrated the importance of representing aerosol nucleation scavenging, impaction or precipitation scavenging, and aerosol regeneration upon evaporation of hydrometeors. They showed that nucleation scavenging accounts for the majority of aerosol removal, but that precipitation scavenging of aerosol can be of importance in many situations. Further, representing the regeneration of aerosols can be quite important in evaporative regions, and it can lead to a significant change in the aerosol distribution size, chemistry, and hygroscopicity or solubility due to aerosol mixing within drops grown by collision–coalescence. More recent work has been done to include these aerosol sources and sinks into more complex aerosol–cloud microphysics models (Ekman et al. 2004, 2006) and to interface these with limited cloud dynamics models (Wang and Chang 1993) so as to provide a more complete representation of aerosols and their impacts on complex cloud systems. Such models are then capable of representing aerosol life cycles and thus more realistically simulate their impacts on clouds. Improvements in the understanding of ice nucleation mechanisms and their representation in numerical models are also of great importance in prediction of ice concentrations, radiation budgets, and frozen precipitation (Fridlind et al. 2007). As such, we have implemented a new scheme for heterogeneous ice nucleation that is based on data from numerous of field studies (DeMott et al. 2010).

The goal of the research presented in this paper is twofold. The first is to present the details of development completed within the RAMS aerosol module with a view to improving the representation of the key sources and sinks of the aerosol life cycle, how they relate to cloud condensation nuclei and ice nuclei (IN), and their links to other microphysical and dynamical processes. The second is to demonstrate the relative importance of the aerosol source and sink mechanisms across cloud scales via an examination of simulated precipitation within raining stratocumulus clouds, deep convection, and orographic snowfall. This manuscript documents the individual modules governing the treatment of aerosols from emissions to activation, scavenging, and regeneration and the radiative impacts of aerosols, as well as the importance of such changes on the surface precipitation of stratiform and

convective precipitation. The inclusion of these individual aerosol representations will allow for more robust studies of aerosol effects over a range of cloud systems. The aerosol modules in RAMS 6.0 are discussed in the following sections.

2. Developments in the treatment of aerosols

a. Aerosol activation and cloud droplet nucleation

There are nine microphysically active aerosol species: 1) submicrometer sulfate, 2) supermicrometer sulfate, 3) submicrometer mineral dust, 4) supermicrometer mineral dust, 5) film-mode sea salt, 6) jet drop-mode sea salt, 7) spume-mode sea salt, 8) submicrometer regenerated aerosols, and 9) supermicrometer regenerated aerosols. Each aerosol spectrum is represented by a lognormal distribution given by

$$N_{\text{aero}}(r_0) = \frac{N_{\text{aero}}}{r_0\sqrt{2\pi}\times\ln\sigma_g}\exp\left[-\frac{(\ln r_0/r_g)^2}{2\ln^2\sigma_g}\right]. \quad (2)$$

Users are allowed to input initial values of aerosol number concentration and mass or median radius of the distributions for any of the aerosol categories, though the regenerated aerosol category is initialized as zero and obtains mass and number as the model microphysics evolves in a given simulation. Sources of dust and sea salt aerosols are also available for use instead of user-prescribed concentration (sections 2d and 2e).

A Lagrangian parcel bin model was run to simulate activation of a distribution of aerosol particles and subsequent nucleation of new cloud droplets. The saturation ratio over an aerosol surface was represented by the Köhler equation as

$$S_{\text{sat}} = \frac{e_r}{e_{\text{sat},w}} = \exp\left[\frac{2M_w\sigma_{s/r}}{\Re T_k\rho_w r_r} - \frac{\nu\phi_s\varepsilon M_w\rho_p r_o^3}{\rho_w M_s(r_r^3 - r_o^3)}\right]. \quad (3)$$

From the Köhler equation, the model first iteratively computes the equilibrium droplet diameters. Parcel simulations are then initialized with chosen aerosol spectra and ambient conditions, and air parcels are lifted just beyond the level of maximum saturation while the droplet growth equation determines the binned sizes of nucleated droplets. The fraction of aerosols that result in newly formed cloud droplets (>2.0-μm diameter) is computed and cataloged. The activation fractions obtained over a range of aerosol characteristics and environmental conditions were used to develop a set of four-dimensional (4D) cloud droplet nucleation lookup tables that vary with vertical velocity, temperature, and aerosol number concentration and median radius.

Given the newly added aerosol species and the potential for large variability in aerosol solubility, we have extended the dimension of the lookup tables to include soluble fraction ε. Ward et al. (2010) and Reutter et al. (2009) represented aerosol solubility with the kappa parameter κ (Petters and Kreidenweis 2007). These studies demonstrated the sensitivity of aerosol activation to the solubility. Rather than using a single ε for all aerosol species, it is most reasonable to allow sea salt aerosols to be nearly fully soluble, while mineral dust may be nearly insoluble; meanwhile, sulfate-based particles could vary over a range of solubility depending on the aerosol source and degree of sulfate coating. The user assigns the aerosol solubility for each species at the time of model initialization, and the solubility remains constant in time for each aerosol category. Figure 1 displays a plot of the percentage of activated aerosols that lead to new droplet nucleation over a range of solubility ε from 5% to 100% and for several values of vertical velocity and aerosol median radius. The solubility has a minimal impact for a situation with 1) strong updrafts and large aerosol median radii (dotted black line) and 2) weak updrafts and small aerosol median radii (solid red line), which represent the upper and lower bounds of the nucleation percentage in the plot. Intermediate combinations of size and updraft lead to larger variations in nucleation with a change in solubility. Permitting variability with ε provides a more accurate representation of aerosols with known chemistry and allows for differentiation among aerosol species.

During the simulated cloud nucleation process, the 4D lookup tables are accessed each time step with the fraction of aerosol number to activate being determined from the five parameters of the lookup tables. For each aerosol species, if the median radius of the distribution is less (greater) than 1 μm at the time of activation, newly nucleated droplets enter the cloud water (drizzle) category. From parcel model results, larger particles tend to result in larger initial droplets that exceed the upper bound on model cloud droplet diameter (2–50 μm) and fit more closely within the drizzle range (50–100 μm).

b. Nucleation scavenging and aerosol regeneration

For a given supersaturated grid cell, each of the aerosol categories competes for potential activation, assuming that the solubility fraction is greater than zero. Relative competition among aerosol categories is based on the total surface area for the number of potentially activated aerosols in each category. The total surface area is computed for each category and then weighted against the sum total surface area of all aerosols. The amount of vapor above saturation that is available for nucleation of new cloud droplets is then divided among the aerosol categories with each given its respective

TABLE 1. List of equation variables and symbols.

Variable	Description
C	Dust scaling factor equal to 1.153×10^{-16} ($\mathrm{g\,s^2\,cm^{-5}}$) that scales emissions to a global annual value of 1851 Tg (Ginoux et al. 2001)
C_c	Cunningham correction factor
C_d	Reference height aerodynamic drag coefficient
d_p,	Diameter of aerosol particle
D	Diameter
D_i	Diameter of size bin i
D_n	Gamma distribution characteristic diameter
D_p	Hydrometeor or raindrop diameter
D_{diff}	Brownian diffusivity of aerosol particle ($\mathrm{m^2\,s^{-1}}$)
D_{dust}	Diameter of dust particles
$E(d_p, D_p)$	Collection efficiency between aerosols and rain drops
E_B	Vegetation surface collection efficiencies for Brownian diffusion
E_{IN}	Vegetation surface collection efficiencies for interception
E_{IM}	Vegetation surface collection efficiencies for impaction
E_{z0}	Erodible surface fraction for dust lofting [Eq. (13)] (Pierre et al. 2012)
e_r	Solution droplet vapor pressure
$e_{\mathrm{sat},w}$	Saturation vapor pressure over a water droplet
F_p	Dust mass flux ($\mathrm{g\,cm^{-2}\,s^{-1}}$)
g	Gravity
G_i	Radiation Mie asymmetry parameter for aerosol type a of bin i
$G_{\mathrm{asym},a}$	Radiation asymmetry parameter for aerosol type a
G_a	Radiation normalized asymmetry parameter of aerosol type a
G_p	Radiation total aerosol asymmetry parameter
k_b	Boltzmann constant ($\mathrm{J\,K^{-1}}$)
k_c	Dry aerosol deposition turbulent transfer velocity term
k_d	Dry aerosol deposition Brownian diffusion and particle slip term
M_{aero}	Total mass of aerosols
M_s	Molecular weight of soluble aerosol material
M_w	Molecular weight of water
$N(D)$	Number concentration of diameter D
N_{aero}	Total number concentration of aerosols
$N_{\mathrm{aero}}(r_0)$	Number concentration of aerosols of dry radius r_0
N_i	Number concentration in size bin i
$N_{\mathrm{dust}}(r_o)$	Number concentration of dust of dry radius r_o
N_{film}	Number concentration of sea salt film drop aerosols ($\mathrm{m^{-3}}$)
N_{jet}	Number concentration of sea salt jet drop aerosols ($\mathrm{m^{-3}}$)
N_{spume}	Number concentration of sea salt spume drop aerosols ($\mathrm{m^{-3}}$)
N_{IN,T_k}	Number concentration ($\mathrm{L^{-1}}$ at STP) of activated IN at temperature T_k
$N_{\mathrm{aer},0.5}$	Number concentration ($\mathrm{cm^{-3}}$ at STP) of aerosols $>0.5\,\mu$m in diameter
N_t	Distribution total number concentration
P	Air pressure (hPa)
P_r	Reference air pressure (1013 hPa)
$Q_{\mathrm{ext},i}$	Radiation Mie extinction coefficient for aerosols of type a and bin size i
$Q_{\mathrm{scat},i}$	Radiation Mie scattering coefficient for aerosols of type a and bin size i
r_m	Mean mass (volume) radius
r_r	Solution droplet equilibrium radius
r_o	Dry aerosol particle radius
r_g	Lognormal distribution geometric median radius
$\Re$	Universal gas constant
R	Rainfall rate for aerosol scavenging
R_b	Surface type rebound factor for aerosol deposition on vegetation surface
$\mathcal{R}_a$	Aerodynamic resistance for aerosol deposition on vegetation surface
$\mathcal{R}_s$	Surface resistance of aerosol deposition on vegetation surface
Re	Reynolds number of raindrop (or any falling hydrometeor)
$\mathrm{Re}_{\mathrm{Dust}}$	Approximated dimensionless friction Reynolds number for dust
S	Sutherland interpolation constant (110.4)
S_{sat}	Köhler equation saturation ratio

TABLE 1. (*Continued*)

Variable	Description
Sc	Schmidt number of aerosol particle
s_p	Relative bin weights of the mass of lofted dust (0.09%, 0.81%, 2.34% 6.76%, 30%, 30%, 30%) expressed as fractions
St	Stokes number of aerosol particle undergoing wet scavenging
St*	Critical Stokes number of aerosol particle undergoing wet scavenging
$\mathrm{St}_{a,\mathrm{water}}$	Stokes number of aerosol particle deposition to a water surface
$\mathrm{St}_{a,\mathrm{veg}}$	Stokes number of aerosol particle deposition to a vegetation surface
T_k	Temperature of air (K)
T_r	Reference temperature (293.15 K)
Δt	Model time step
κ	Von Kármán constant (0.4)
u	Wind speed at the first model level above ground
u_*	Wind friction velocity related to surface roughness
u_h	Reference height wind speed at 10 m AGL
u_t^*	Threshold wind friction velocity for dust
$u_{t,\mathrm{wet}}^*$	Wet soil threshold friction wind velocity for dust
$v(d_p)$	Terminal velocity of aerosol particle
$V(D_p)$	Terminal velocity of raindrop (or any falling hydrometeor)
$V_{d,\mathrm{water}}$	Dry deposition onto a water surface
$V_{d,\mathrm{veg}}$	Dry deposition of aerosol particles onto a vegetation or soil surface
V_g	General aerosol gravitational settling velocity
$V_{g,\mathrm{dry}}$	Dry aerosol gravitational settling velocity
$V_{g,\mathrm{wet}}$	Wet aerosol gravitational settling velocity
w	Total volumetric soil moisture ($\mathrm{m^3\,m^{-3}}$) as percent
w'	Volumetric soil moisture ($\mathrm{m^3\,m^{-3}}$) at maximum adsorption as percent
W	Vertical velocity ($\mathrm{m\,s^{-1}}$)
z_0	Surface roughness length
$z_{0,\mathrm{veg}}$	Vegetation roughness length
Δz	Distance from the surface to the first model level
$\beta_{\mathrm{ext},a}$	Radiation aerosol extinction of aerosol type a
$\beta_{\mathrm{scat},a}$	Radiation aerosol scattering of aerosol type a
ε	Fraction of aerosol soluble material
$\Gamma(v)$	Gamma function of width v
$\Lambda(d_p)$	Aerosol scavenging coefficient
λ	Molecular mean free path of air (m)
λ_r	Reference molecular mean free path of air (0.0651×10^{-6} m)
η_r	Reference dynamic air viscosity ($1.8205 \times 10^{-5}\,\mathrm{kg\,m^{-1}\,s^{-1}}$)
ρ_a	Density of air
ρ_p	Density of aerosol particle
ρ_w	Density of water
σ_g	Lognormal distribution geometric standard deviation
$\sigma_{s/r}$	Solution droplet surface tension
τ	Relaxation time of wet scavenged aerosol particle
τ_a	Radiation optical depth for aerosols of type a
τ_p	Radiation total aerosol optical depth
τ_{salt}	User-chosen sea salt regeneration relaxation time
μ_a	Dynamic viscosity of air ($\mathrm{kg\,m^{-1}\,s^{-1}}$)
μ_w	Viscosity of water ($\mathrm{kg\,m^{-1}\,s^{-1}}$)
μ_a/ρ_a	Kinematic viscosity of air
ν	Gamma distribution shape parameter
$\nu\phi_s$	Number of dissociated ions in solution × molal osmotic coefficient
ω_a	Radiation single scatter albedo for aerosols of type a
ω_p	Radiation total aerosol single scatter albedo

weighting. From the total distribution aerosol particle mass and number concentration, we can relate the mean mass (volume) radius to the median radius of the lognormal distribution that is used for computing the nucleation lookup tables. This relationship is given as

$$r_m = r_g \exp(1.5 \ln^2 \sigma_g). \quad (4)$$

A distribution width of $\sigma_g = 1.8$ was assumed for the aerosol spectra used in the creation of the nucleation lookup tables (similar to Saleeby and Cotton 2004a).

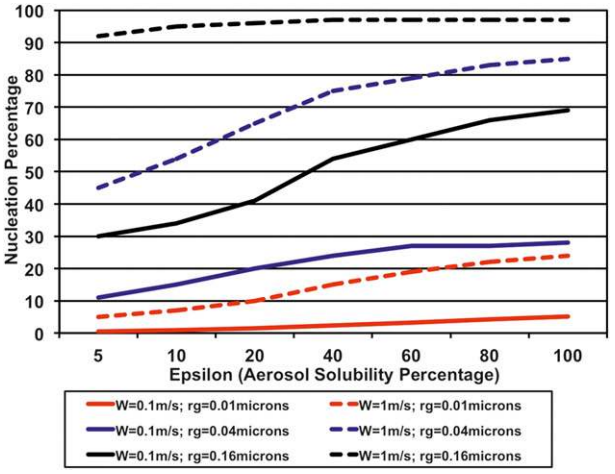

FIG. 1. Percentage of activated aerosol particles that result in cloud droplet nucleation as a function of the aerosol solubility percentage (ε), vertical velocity (W), and median radius of the aerosol distribution (r_g). The number concentration was set at $1000\,\mathrm{cm}^{-3}$.

Given this relationship between the mean radius and median radius, the median radius for a certain mass and number of aerosols can then be computed as

$$r_g = \frac{\left(\frac{3}{4\pi\rho_p}\frac{M_{\text{aero}}}{N_{\text{aero}}}\right)^{1/3}}{\exp(1.5\ln^2\sigma_g)}. \quad (5)$$

The aerosol density is a free parameter to be set by the user but is initially assigned the following default values: sulfate ($1.769\,\mathrm{g\,cm}^{-3}$), submicrometer mineral dust (clay $2.500\,\mathrm{g\,cm}^{-3}$), supermicrometer mineral dust (silt $2.650\,\mathrm{g\,cm}^{-3}$), and sea salt ($2.165\,\mathrm{g\,cm}^{-3}$). By knowing number, mass, and median radii of the various aerosol type categories, the aerosol distributions can be computed at the time of new cloud droplet nucleation. The lognormal distributions are partitioned into 100 bins over an optimized size range that is specific for a given median radius. The initial implementation of aerosol removal, via nucleation scavenging in Saleeby and Cotton (2004a), did so from an aerosol distribution of 200 bins that covered a single size range that included all aerosol mass and numbers for median radii from 0.01 to 0.96 μm. This representation of the distribution results in low bin resolution that can sometimes produce discrepancies when trying to match bin mass and number for aerosol removal. In the updated scheme we established discrete distribution bin size ranges for each represented median radius in both the Lagrangian parcel model and the representation of the lognormal distributions used within RAMS. This improves bin resolution and allows us to precisely encompass the aerosol mass and number within this range without having wasted bin space. It also eliminates the need for the 200 size bins and specified distribution truncation initially employed by Saleeby and Cotton (2004a) to handle the discrepancy between the aerosol mass and number distributions. Upon binning the distribution, the aerosol number and mass that participate in nucleation are removed from the environment by subtracting the nucleated number concentration from the large end of the aerosol distributions since the larger particles are preferentially activated over those at the small end of the distribution. Following this subtraction, an updated median radius is computed, which will be a smaller value than that prior to nucleation. Since this is a bin-emulating approach, the remaining aerosol number and mass are redistributed according to the lognormal basis function based on the newly computed median radius.

Upon nucleation of new cloud droplets, the aerosol mass that is removed from the aerosol population is transferred to a 3D scalar variable that is used to track the amount of total aerosol mass *contained within* cloud droplets, called *aerosol in cloud*. This mass is a conglomerate of all aerosol types consumed during nucleation. There is a different 3D scalar tracking variable associated with each hydrometeor type so as to allow transfers of *aerosol mass in hydrometeors* among hydrometeor categories whenever transfers of condensate mass occur from one hydrometeor category to another. During the condensate mass transfers that would occur during collision–coalescence, freezing, or melting, the aerosol mass in hydrometeors is transferred in proportion to the amount of transferred hydrometeor mass. So, for example, if 50% of the hail mass melts in a given grid cell and becomes rain, then 50% of the aerosol mass contained within hail particles, referred to as *aerosol mass in hail*, will be transferred to the *aerosol mass in rain* category. This method of tracking aerosol mass contained within hydrometeors is similar to the aerosol mass ratio transfer scheme of Rutledge et al. (1986) and Hegg et al. (1986).

When grid cells containing hydrometeors undergo evaporation, a number of precipitation particles may fully evaporate and restore aerosols back to the environment. The amount of restored aerosol mass is in proportion to the amount of mass of fully evaporated hydrometeors relative to the total hydrometeor mixing ratio. If the mass of the fully evaporated hydrometeors in a given hydrometeor category is 10% of the total hydrometeor mass in that category, then 10% of the tracked aerosol mass within that hydrometeor species is restored to one of the regenerated aerosol categories. The number of restored aerosols equals the number of fully evaporated hydrometeors. From the restored aerosol mass and number,

Eq. (5) is used to compute the median radius of the regenerated aerosols. If the median radius is less than (greater than) 1 μm, then the aerosols are returned to the submicrometer (supermicrometer) regenerated aerosol category. By not restoring aerosols back to a parent category, we can examine the spatial and temporal changes in the initial aerosol categories. It should be noted that the regenerated aerosols must be given a constant solubility fraction. A reasonable approximation could be computed as the mass-weighted solubility of the total initial aerosol distributions.

Figure 2 displays a cross section of the number concentration of submicrometer sulfate aerosols and regenerated aerosols through the main updraft of an idealized deep convective storm at 2 h into the test simulation (similar to Saleeby and Cotton 2004a). The model was initialized with 3D homogenous aerosol number concentrations of 1000 cm^{-3} and a median radius of 0.04 μm in the submicrometer sulfate category only. Other aerosol species were initialized with zero concentration. There is a distinct area of aerosol nucleation scavenging (reduced aerosol concentration) where the center of the updraft resides. Regenerated aerosols are concentrated near and below cloud base (2–3 km) and along the edges of the updraft (up to 11 km). It is likely that the modest amount of aerosol regeneration along the region where cloud edges would exist at mid to upper levels is a result of turbulent mixing and entrainment. Engström et al. (2008) found similar regions of aerosol regeneration along cloud boundaries because of mixing with dry air. The greatest zone of aerosol regeneration is to the rear of the storm (left side), where the convective downdraft resides and enhanced subsidence increases evaporation of hydrometeors.

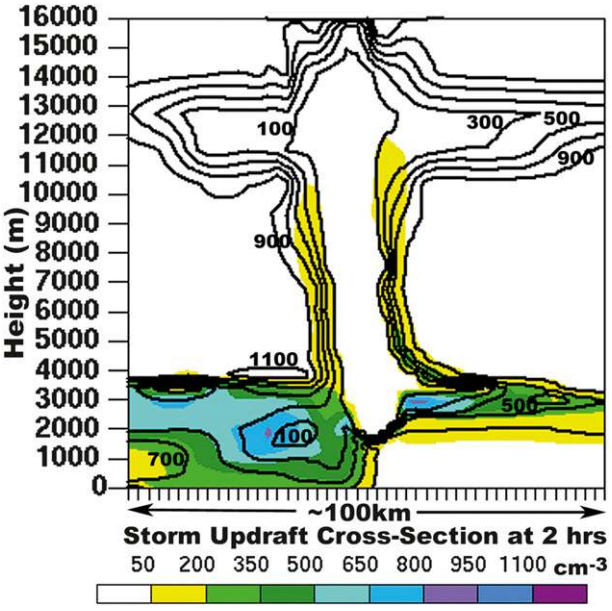

FIG. 2. Vertical cross section through a storm updraft (at 2-h simulation time) showing the number concentration of unprocessed aerosols (cm^{-3}, black contours) and regenerated aerosols (cm^{-3}; color shading). The aerosol concentration was 3D homogeneously initialized at 1000 cm^{-3} so as to better view the effects of the removal by nucleation scavenging and aerosol regeneration. (Only the submicrometer sulfate aerosol category was active, and aerosol dry and wet deposition were inactive.)

c. *Heterogeneous ice nucleation*

The parameterization of heterogeneous ice nucleation implemented here is from DeMott et al. (2010). Their active IN formulation is based on observations from nine field projects collected over 14 years across a wide range of locations. Observations were taken with the CSU Continuous Flow Diffusion Chamber in water-saturated conditions (relative humidity $>$ 100%). As such, this technique captures ice particles nucleated via deposition nucleation, condensation freezing, and immersion freezing. A strong correlation was found between IN concentration and the concentration of aerosol particles with diameters greater than 0.5 μm. The DeMott formula, given as

$$N_{\mathrm{IN},T_k} = a(273.16 - T_k)^b (N_{\mathrm{aer},0.5})^{[c(273.16-T_k)+d]}, \qquad (6)$$

where $a = 0.000\,059\,4$, $b = 3.33$, $c = 0.0264$, and $d = 0.0033$, is a power law fit to these data and represents the maximum number of IN activated down to a temperature of −35°C. Number concentrations in Eq. (6) are specified at standard temperature and pressure (STP). This equation takes into consideration all sampled aerosol species, which includes aerosols with different chemical compositions as well as insoluble mineral dust. Figure 3 displays plots of the DeMott formula at −15°, −25°, and −35°C. The trend toward greater IN activation at colder temperatures is evident. To apply the DeMott formula in RAMS, we determine the median radius for each of the non–sea salt aerosol categories, decompose the distributions into binned lognormal spectra, and sum the total number of aerosols greater than 0.5-μm diameter. The formula then determines the number of activated particles, which are then removed from the available population as ice particles are generated. Particles are activated and removed from largest to smallest. New ice mass is generated up to the amount of available water mass above water saturation.

It should be noted that the DeMott formula provides the *maximum* number of activated IN for a given temperature. Once the formula is applied at a certain model grid point it cannot be directly reapplied at this location in the subsequent model time step unless conditions are colder or more saturated so as to support additional

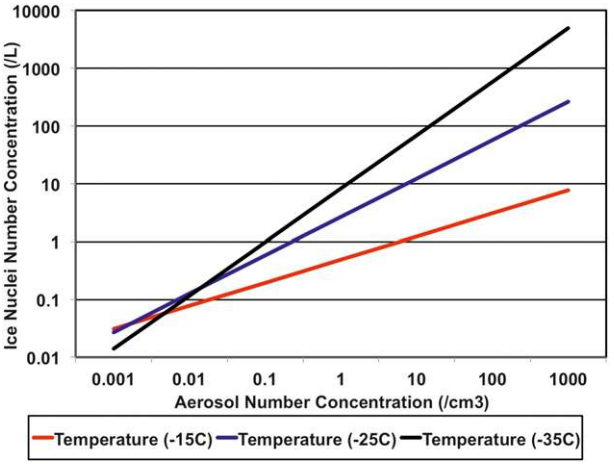

FIG. 3. Activated ice nuclei number concentration (L^{-1}) shown as a function of aerosol number concentration (cm^{-3}) and environment temperature (°C) from the DeMott et al. (2010) equation for heterogeneous ice nucleation.

nucleation; otherwise, overnucleation of IN occurs. To prevent overnucleation, the number of activated IN are tracked within the model. The IN tracking variable is treated as a new 3D scalar variable with predictive tendencies computed accordingly throughout the model. By knowing the number of activated and unactivated IN at a given location, we can determine if additional ice nucleation should occur for the given ambient conditions.

It should be noted here that, while the DeMott formula is not active in water subsaturated conditions, the microphysics model simulates contact nucleation, homogeneous freezing of cloud droplets, and homogeneous freezing of deliquesced, but unactivated, haze particles (Walko et al. 1995). Furthermore, the user retains the option to use the Meyers et al. (1992) formula, which allows water subsaturated activation of IN.

d. Sea salt model

A model for the prediction of sea salt aerosols has been implemented (Carrio and Cotton 2011). Emission of sea salt particles from the ocean surface is a function of wind-driven processes. O'Dowd et al. (1997, 1999) provide empirical relationships between near-surface wind speed over the ocean and the concentration of sea salt aerosols. They divided the sea salt aerosol distribution into three naturally occurring modes: 1) a spume drop mode of ultragiant particles with mode radius of $r_g = 6.0\,\mu$m that is generated from the shearing of wave crests, 2) a jet drop mode ($r_g = 1.0\,\mu$m) that is formed from small jets that are emitted from bursting bubbles in the foam top of white caps, and 3) a film drop mode ($r_g = 0.1\,\mu$m) that forms from the film of the bursting bubbles that generate the jet drops. The numerical relationships for the number concentration of the three modes, based on the 10-m wind speed, are given (in mks units) as

$$\begin{aligned} N_{\text{film}} &= 10^{(0.095u_h+6.283)}, \\ N_{\text{jet}} &= 10^{(0.0422u_h+5.7122)}, \quad \text{and} \\ N_{\text{spume}} &= 10^{(0.069u_h+0.19)} \end{aligned} \tag{7}$$

with

$$u_h = u\frac{\ln(10_m/z_0)}{\ln(\Delta z/z_0)}. \tag{8}$$

O'Dowd et al. (1999) compiled these relationships for wind speeds from 2 to 17 $m\,s^{-1}$, Fan and Toon (2011) presented sea salt emissions for wind speeds up to 20 $m\,s^{-1}$, and Smith et al. (1993) provided spume emissions for winds speeds up to 32 $m\,s^{-1}$. As such, we apply an upper wind speed limit of 20 $m\,s^{-1}$ for the film and jet modes and 32 $m\,s^{-1}$ for the spume mode so as to prevent overproduction of sea salt in high wind conditions. When implementing Eq. (7) for sea salt number concentration, we apply these values to the lowest model level above ground. If mixing or deposition reduces the salt concentrations at the surface, we apply a time weighted tendency function, acting on a time scale of $\Delta t/\tau_{\text{salt}}$, to bring the concentrations back to the predicted values.

Figure 4 displays a vertical cross section of the number concentration of particles in the film sea salt mode resulting from emissions due to strong surface winds associated with convective downdraft outflow over an ocean surface (the same test simulation as used in Fig. 2, but here with an ocean surface). These results occurred during the mature phase of the convection when near-surface horizontal winds were strong. The top (bottom) panel displays the concentrations that result without (with) the maximum wind speed limit of 20 $m\,s^{-1}$. There is a maximum source region of sea salt particles near the peak in the surface wind speed, and some of the emitted particles are drawn into the updraft. Without the wind speed limit, number concentrations become twice as large.

e. Dust aerosol source model

A model for dust lofting from an arid surface based on soil moisture, wind speed, and soil clay percentage has been implemented in RAMS (Smith 2007; Seigel and van den Heever 2012). For bare soil surfaces, there exists a wind threshold friction velocity required to overcome soil cohesion forces and allow soil particles to separate and loft from the surface. Marticorena and Bergametti (1995) fitted relationships to experimental data to parameterize the threshold wind friction velocity, u_t^* ($cm\,s^{-1}$) in cgs units as

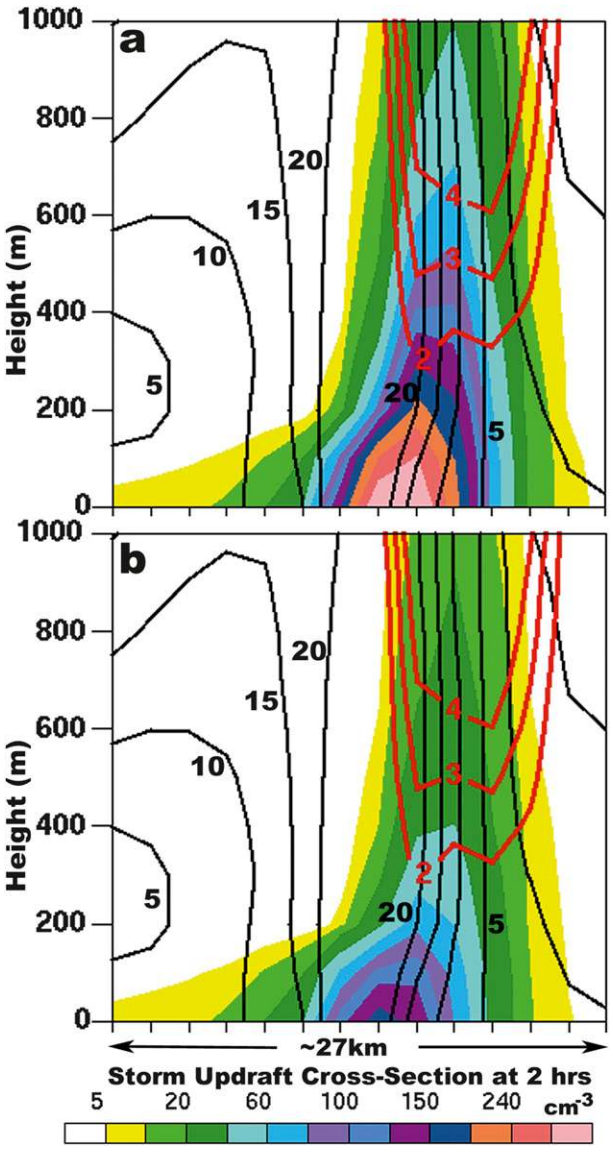

FIG. 4. Vertical cross sections of the number concentration of film-mode sea salt aerosols (mode radius = 0.1 μm; cm^{-3}; color shaded), horizontal wind speed (m s^{-1}; black contours), and vertical velocity (m s^{-1}; red contours) near the peak outflow winds of a simulation of deep convection after 2 h of simulation time. The parameterization was implemented such that the wind speed used in the source equations is (a) not limited or (b) limited to 20 m s^{-1}.

$$u_t^* = \frac{0.13K}{\sqrt{1.928\mathrm{Re}_{\mathrm{Dust}}^{0.092} - 1}},$$

$$K = \sqrt{\left(\frac{\rho_p g D_{\mathrm{dust}}}{\rho_a}\right)}\sqrt{\left(1 + \frac{0.006}{\rho_p g D_{\mathrm{dust}}^{2.5}}\right)}, \quad \text{and}$$

$$\mathrm{Re}_{\mathrm{Dust}} = 1331 D_{\mathrm{dust}}^{1.56} + 0.38. \tag{9}$$

Note that there is an inverse relationship between particle size and the threshold friction velocity. Smaller particles require a larger wind speed to overcome cohesion forces. Alfaro and Gomes (2001) and Shao (2001) have taken a similar approach, while recent work by Kok (2011) suggests that size-specific dust emission does not vary with threshold friction velocity. However, as model wind speeds are increased beyond the range of the threshold friction velocity [~(0.5–2.5) m s^{-1}] the change in the emitted particle size distribution decreases, and the differences in these parameterizations are minimized.

Soil cohesion and the threshold friction velocity are also a function of soil type and soil moisture. Water in the soil increases capillary forces that bond particles together and enhance cohesion (Fécan et al. 1999). However, the adsorption capacity of the soil determines when the water capillary forces become strong enough to enhance cohesion. The soil has to reach adsorption capacity before cohesion increases, and subsequently stronger wind speeds are needed for lofting. From Fécan et al. (1999), the volumetric soil moisture (m^3 m^{-3}) at maximum adsorption is a function of clay content, given as

$$w' = 0.0014(\%\mathrm{clay})^2 + 0.17(\%\mathrm{clay}), \tag{10}$$

where "% clay" refers to the fraction of clay composition within a given soil type, expressed as a percent. The wet soil threshold friction wind velocity (in cgs units) is

$$u_{t,\mathrm{wet}}^* = \begin{cases} u_t^*\sqrt{[1 + 1.21(w - w')^{0.68}]} & \text{for} \quad w > w' \\ u_t^* & \text{for} \quad w < w' \end{cases}. \tag{11}$$

Soils with higher clay content can be lofted more easily for a given wind speed because of the enhanced ability to adsorb water and limit interparticle cohesion from water capillary tension. Table 2 displays the soil types in the Land Ecosystem–Atmosphere Feedback, version 3 (LEAF-3), land surface model [the former version, LEAF-2, is documented in Walko et al. (2000b)] along with the maximum volumetric soil moisture (m^3 m^{-3}) and clay percentage.

We represent lofting of dust particles across seven particle radius bins (0.15, 0.26, 0.47, 0.83, 1.50, 2.65, and 4.71 μm) since there may be variability in lofting with size (Tegen and Fung 1994; Tegen and Lacis 1996; Ginoux et al. 2001). Dust mass flux F_p (g cm^{-2} s^{-1}) in each size bin follows Ginoux et al. (2001) (in cgs units) as

$$F_p = \begin{cases} E_{z0} C s_p u_h^2 (u_h - u_{t,\mathrm{wet}}^*) & \text{for} \quad u_h > u_{t,\mathrm{wet}}^* \\ 0 & \text{otherwise} \end{cases} \tag{12}$$

and

$$E_{z0} = \begin{cases} 1 & \text{if} \quad z_{0,\text{veg}} < 3 \times 10^{-3}\,\text{cm} \\ 0.7304 - [0.0804 \log_{10}(z_{0,\text{veg}})] & \text{if} \quad z_{0,\text{veg}} > 3 \times 10^{-3}\,\text{cm} \end{cases}. \tag{13}$$

Greater roughness length reduces the erodible fraction and the amount of dust lofting. Table 3 displays the vegetation land surface classes that may act as dust lofting sources as well as the vegetation roughness length, vegetation height, and total leaf area index (TAI). (TAI values are representative of the summer growing season. The roughness length for certain vegetation classes will vary as the TAI varies during seasonal changes.) Dust lofting is not active for surface patches covered by snow or for the vegetation classes of ocean, inland water, ice, marshes, wetland trees, or highly urban.

The mass flux in each size bin is converted into number concentrations of newly lofted dust within the first model layer above ground in a given time step (in cgs units) as

$$N_{\text{dust}}(r_o) = \frac{F_p \Delta t/\Delta z}{(4/3)\pi \rho_p r_o^3}. \tag{14}$$

The four (three) smallest (largest) size bins are summed to comprise the submicrometer (supermicrometer) dust category with median radius of 0.69 (2.95) μm. Figure 5 displays the surface dust flux as it varies with soil moisture, clay percentage, and 10-m wind speed. Dust flux increases with a decrease in soil moisture, increase in soil clay percentage, and increase in wind speed. The greatest variability occurs with wind speed, then with soil moisture, and least with clay percentage. Seigel and van den Heever (2012) demonstrated the utility of this dust lofting mechanism and showed that resulting dust concentrations are similar to those observed during an intense dust storm in the southwest United States.

f. Aerosol wet deposition (precipitation scavenging)

An aerosol wet deposition (precipitation scavenging) scheme was initially implemented by Smith (2007) in RAMS 4.3 that accounts for scavenging by rain drops in the subcloud layer based on the surface rain rate. It has since been integrated into RAMS 6.0 and is applied to each of the nine aerosol species. It has been extended to additionally consider precipitation scavenging within clouds by all hydrometeor species with the use of 3D precipitation rates. Precipitation particles falling through the atmosphere collide with aerosol particles and collect a portion of them. Higher precipitation rates lead to greater collection and removal of aerosol particles. The rainfall scavenging coefficient for a monodisperse population of raindrops, presented by Seinfeld and Pandis (2006) and Wang et al. (2010) and based on Slinn (1983), is computed (in mks units) as

$$\Lambda(d_p) = \frac{3E(d_p, D_p)R}{2D_p}. \tag{15}$$

The aerosol diameter used here is the wet or deliquesced aerosol diameter computed from the dry diameter as a function of relative humidity, according to Fitzgerald (1975).

The size specific collection efficiency $E(d_p, D_p)$ between aerosols and raindrops is a function of three primary collection mechanisms: Brownian diffusion, interception, and inertial impaction (Slinn 1983; Seinfeld and Pandis 2006; Berthet et al. 2010; Wang et al. 2010). Collection by Brownian diffusion is a function of random motions that bring aerosols in contact with falling drops, and as such, decreases with increasing aerosol particle size; it is most effective for aerosols with diameter less than 0.2 μm. Interception occurs primarily for intermediate size particles ($0.2 < d_p < 1.0\,\mu$m). This method occurs as aerosols follow the airflow streamlines around a drop. These aerosols are of small enough mass that they tend not to cross flow-field streamlines; only particles that come within a half diameter distance of the drop will collide. This method is the most inefficient of the three. Inertial impaction occurs for larger aerosols ($d_p > 1.0\,\mu$m). The flow of these aerosols is more a function of the mass rather than the diameter; aerosols with larger mass have a greater inertia and can cross flow-field streamlines as falling drops scavenge out a volume of air. Given the greater dependence on mass, higher density aerosols are scavenged more efficiently at smaller diameters than lower density particles. The collection efficiencies are computed (in mks units) as

$$\begin{aligned} E(d_p, D_p) \quad &[\text{collection efficiency } (0 < E < 1)] = \\ &\frac{4}{\text{ReSc}}(1 + 0.4\text{Re}^{1/2}\text{Sc}^{1/3} + 0.16\text{Re}^{1/2}\text{Sc}^{1/2}) \\ &\qquad \text{(Brownian diffusion contribution)} \\ &+ 4\frac{d_p}{D_p}\left[\frac{\mu_a}{\mu_w} + (1 + 2\text{Re}^{1/2})\frac{d_p}{D_p}\right] \\ &\qquad \text{(interception contribution)} \\ &+ \sqrt{\frac{\rho_p}{\rho_w}} \times \left(\frac{\text{St} - \text{St}*}{\text{St} - \text{St}* + 2/3}\right)^{3/2} \\ &\qquad \text{(inertial impaction contribution)}, \end{aligned} \tag{16}$$

TABLE 2. RAMS soil type and characteristics for soil dust particle lofting.

Soil type	Saturation volumetric soil moisture ($m^3\,m^{-3}$)	Clay percentage (%)
Sand	0.395	0
Loamy sand	0.410	5
Sandy loam	0.435	10
Silt loam	0.485	12
Loam	0.451	18
Sandy clay loam	0.420	28
Silty clay loam	0.477	33
Clay loam	0.476	33
Sandy clay	0.426	42
Silty clay	0.492	48
Clay	0.482	70
Peat	0.863	0

TABLE 3. RAMS vegetation type and roughness length used for dust lofting suppression (based on TAI for summer season).

Vegetation type	LEAF-3 class	Roughness length (m)	Vegetation height (m)	TAI
Evergreen needleleaf tree	4	2.35	20.0	4.11
Deciduous needleleaf tree	5	2.59	22.0	4.11
Deciduous broadleaf tree	6	2.26	22.0	1.88
Evergreen broadleaf tree	7	3.50	32.0	2.86
Short grass	8	0.03	0.3	3.28
Tall grass	9	0.14	1.2	4.04
Semidesert	10	0.07	0.7	0.58
Tundra	11	0.02	0.2	2.41
Evergreen shrub	12	0.11	1.0	3.15
Deciduous shrub	13	0.11	1.0	3.15
Mixed woodland	14	2.36	22.0	2.57
Crop/mixed farming	15	0.10	1.0	1.41
Irrigated crop	16	0.11	1.1	1.41
Wooded grassland	18	0.73	7.0	2.01
Urban and built-up	19	0.60	6.0	1.53

where

$$\mathrm{Re} = \frac{D_p V(D_p)\rho_a}{2\mu_a}, \quad \mathrm{Sc} = \frac{\mu_a}{\rho_a D_{\mathrm{diff}}},$$

$$D_{\mathrm{diff}} = \frac{k_b T_k C_c}{3\pi\mu_a d_p}, \quad \mathrm{St} = \frac{2\tau[V(D_p) - v(d_p)]}{D_p},$$

$$\tau = \frac{(\rho_p - \rho_a) d_p^2 C_c}{18\mu_a}, \quad \mathrm{St}^* = \frac{1.2 + (1/12)\ln(1 + \mathrm{Re})}{1 + \ln(1 + \mathrm{Re})},$$

$$C_c = 1 + \frac{2\lambda}{d_p}\left[1.257 + 0.4\exp\left(-0.55\frac{d_p}{\lambda}\right)\right],$$

$$\mu_a = \eta_r \left(\frac{T_r + S}{T_k + S}\right)\left(\frac{T_k}{T_r}\right)^{3/2},$$

and

$$\lambda = \lambda_r \left(\frac{P_r}{P}\right)\left(\frac{T_k}{T_r}\right)\left(\frac{1 + S/T_r}{1 + S/T_k}\right).$$

This equation set [Eq. (16)] computes a collection efficiency value based on single aerosol and raindrop sizes; however, in the absence of a bin model, the RAMS bulk microphysics model uses hydrometeor gamma distributions and aerosol lognormal distributions. To apply the collection efficiency and scavenging coefficient equations to RAMS, we must use the mean raindrop diameter for D_p and the median aerosol diameter for d_p as reasonable approximations to represent these bulk quantities in the size-specific scavenging equations. Power-law relationships for raindrop mass and fall speed are used for computing collection efficiencies. The application of Eq. (16) to Eq. (15) provides the scavenging coefficients for a range of aerosol particle sizes, particle densities, and raindrop sizes (Fig. 6). We extend this scavenging approach to ice hydrometeors by assuming them to be spheres for Eq. (16), although power-law coefficients for mass and fall speed are ice habit specific. Seinfeld and Pandis (2006) suggest that the aerosol collection efficiencies for ice hydrometeors with complex shapes may be higher than for spheres. Therefore, our implementation for scavenging by ice particles may represent a lower bound on scavenging in cold and mixed-phase clouds.

For verification, Fig. 6 displays scavenging rates for aerosol particle collection at a rainfall rate of $1\,\mathrm{mm\,h^{-1}}$. These are in good agreement with Wang et al. (2010) and Seinfeld and Pandis (2006). A demonstration of scavenging is shown in Fig. 7 for the collection of 3-μm diameter dust aerosols by precipitation hydrometeors along a transect through the main updraft within our deep convection simulation. We have isolated the precipitation scavenging process by not allowing dust to be removed by nucleation scavenging. Figure 7a (Fig. 7b) reveals dust number concentrations near the main updraft of the storm without (with) scavenging. The initial dust concentration vertical profile can be seen in the lower levels of the undisturbed region to the right of the updraft. Without scavenging, these large dust particles are transported from the boundary layer into the updraft and diverge into the anvil region. With active scavenging, precipitation in the updraft removes the dust, thereby preventing dust from reaching high concentrations at upper levels. Though not shown, plots of the

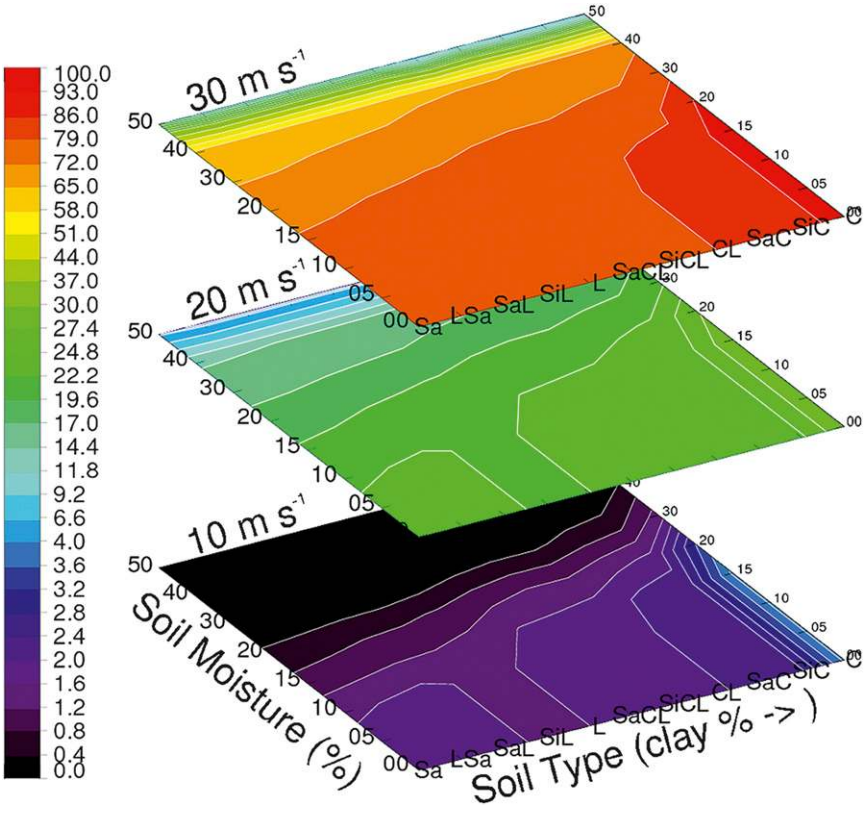

FIG. 5. Flux of dust lofted from the surface ($cm^{-3}\,s^{-1}$) as a function of soil type clay composition (%), soil moisture (%), and 10-m wind speed ($m\,s^{-1}$). Figure is courtesy of R. B. Seigel; adapted from work by Seigel and van den Heever (2012).

scavenging of smaller particles with lower scavenging rates showed less aerosol removal and more transport to the anvil. It is important to also note that aerosols subject to precipitation scavenging are tracked within hydrometeor species and can be regenerated by hydrometeor evaporation.

g. *Aerosol dry deposition (gravitational settling)*

The fall speed of settling aerosol particles results from a balance between gravitational and atmospheric drag forces. First, we compute the wet particle size from the dry particle size, aerosol solubility fraction, and relative humidity according to Fitzgerald (1975). From Baron and Willeke (2001) and Seinfeld and Pandis (2006), the gravitational settling velocity through atmospheric layers above the first model layer is expressed for the Stokes regime (particle Reynolds numbers <0.1), as

$$V_g = \frac{\rho_p d_p^2 g C_c}{18\mu_a}. \tag{17}$$

Here d_p is the aerosol wet particle diameter. The aerosol distribution mean fall velocity is based on the bulk lognormal distribution median diameter and is applied equally to the settling of aerosol mass and number down to the second model layer above ground. The dry deposition of particles in the first model layer is additionally subject to surface characteristics and surface layer turbulence effects.

Slinn and Slinn (1980) addressed dry deposition onto a water surface. For calm winds the deposition velocity equals the gravitational settling velocity. For nonzero winds in the surface layer, the deposition velocity can be expressed (in mks units) as

$$V_{d,\text{water}} = 1 \Big/ \left(\frac{1}{k_c} + \frac{1}{k_d} - \frac{V_{g,\text{dry}}}{k_c k_d} \right), \tag{18}$$

where

$$k_c = V_{g,\text{dry}} + \frac{1}{1-\kappa} C_d u_h \quad \text{and} \tag{19}$$

$$k_d = V_{g,\text{wet}} + \frac{1}{\kappa} C_d u_h (\text{Sc}^{-1/2} + 10^{-3/\text{St}_{a,\text{water}}}), \tag{20}$$

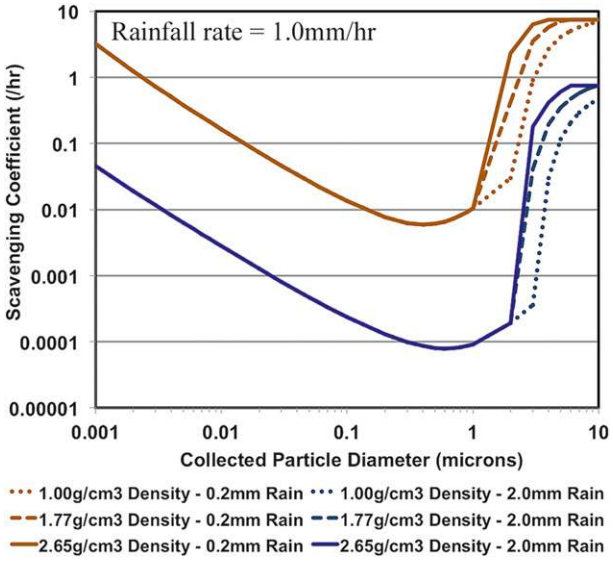

FIG. 6. Aerosol scavenging coefficient (h^{-1}) plotted as a function of collected aerosol particle diameter, aerosol density, and rain drop diameter. A density of 1.00 g cm^{-3} represents the baseline formulation for the collection efficiency, and densities of 1.77 and 2.65 g cm^{-3} are representative of ammonium sulfate and mineral dust. Note that the curves representing the same rain drop size overlap except in the supermicrometer range where inertial impaction is dominant.

with

$$C_d = \frac{u_*^2}{u_h^2} \quad \text{and} \quad \mathrm{St}_{a,\mathrm{water}} = \frac{V_{g,\mathrm{wet}}}{g}\frac{u_*^2}{\mu_a/\rho_a}. \qquad (21)$$

The dry deposition of aerosol particles onto a vegetation or bare soil surface is parameterized according to Slinn (1982) and Zhang et al. (2000) (in mks units) as

$$V_{d,\mathrm{veg}} = V_{g,\mathrm{wet}} + \frac{1}{\mathcal{R}_a + \mathcal{R}_s}, \qquad (22)$$

where

$$\mathcal{R}_a = \frac{u_h}{u_*^2} \quad \text{and} \quad \mathcal{R}_s = \frac{1}{\varepsilon_0 u_* R_b (E_B + E_{\mathrm{IN}} + E_{\mathrm{IM}})}, \qquad (23)$$

and ε_0 is a constant of 3.0. The vegetation surface collection efficiencies (E_x) are

$$E_B = \mathrm{Sc}^{-\gamma} \quad \text{(Brownian diffusion)},$$

$$E_{\mathrm{IN}} = \frac{1}{2}\left(\frac{d_p}{A}\right)^2 \quad \text{(interception), and}$$

$$E_{\mathrm{IM}} = \left(\frac{\mathrm{St}_{a,\mathrm{veg}}}{\alpha + \mathrm{St}_{a,\mathrm{veg}}}\right)^{\beta} \quad \text{(impaction)}. \qquad (24)$$

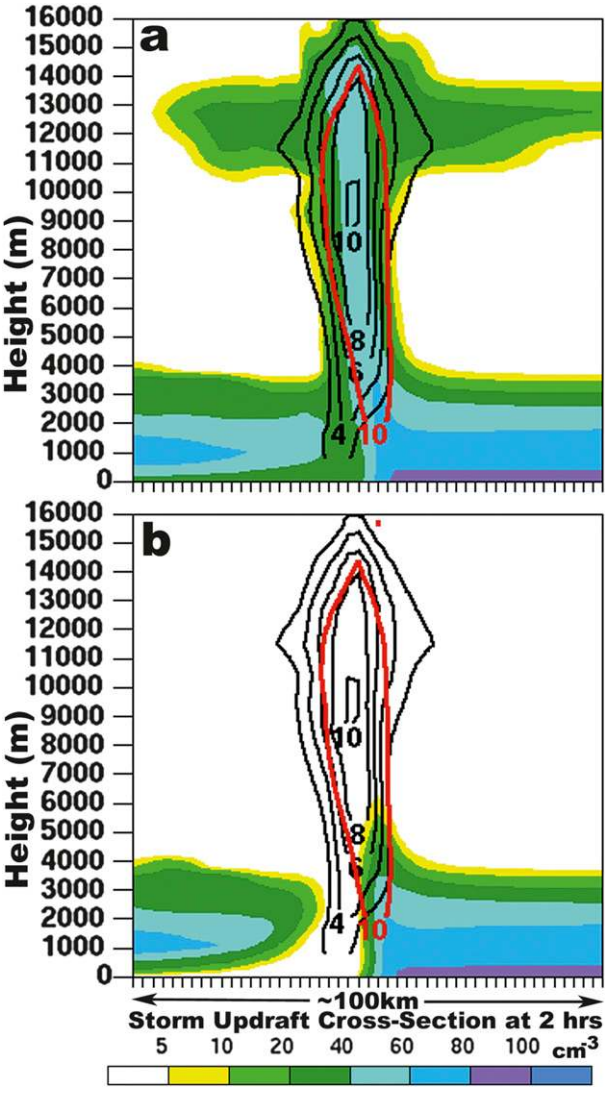

FIG. 7. Vertical cross section through a storm updraft (at 2-h simulation time) showing the 10 m s^{-1} vertical velocity contour (red line), total condensate (g kg^{-1}; black contours), and number concentration of dust from the large-particle dust mode with median diameter of 3 μm (cm^{-3}; color shaded) in circumstances of (a) wet deposition turned off and (b) wet deposition turned on. The dust concentration along the far right side of the plot in the lower levels is indicative of the domainwide initial profile.

Here

$$R_b = \exp(-\mathrm{St}_{a,\mathrm{veg}}^{1/2}) \quad \text{(surface rebound factor)} \qquad (25)$$

and

$$\mathrm{St}_{a,\mathrm{veg}} = \frac{V_{g,\mathrm{wet}}}{g}\frac{u_*}{A} \quad \text{(vegetation Stokes number)}, \qquad (26)$$

where γ, A, α, and β are empirical constants that vary with surface types given by Zhang et al. (2000). The vegetation Stokes number is used for vegetation surfaces only and reduces to the Stokes parameter in Eq. (21) for nonvegetative surfaces, R_b reduces to 1.0 for water, and E_{IN} reduces to 0.0 for nonvegetative surfaces (desert, tundra, water, and ice).

Figure 8 displays the aerosol dry deposition velocities from gravitational settling and deposition onto water and vegetation for a range of aerosol sizes. This plot agrees well with the results from Slinn and Slinn (1980) for deposition onto water, and from Slinn (1982) and Zhang et al. (2000) for deposition onto vegetation. Note that the gravitational settling velocity of submicrometer-diameter particles in the free atmospheric is substantially lower than surface deposition. The increase in surface dry deposition of particles $>\sim 1\,\mu$m in diameter is from the increased effects of inertial impaction.

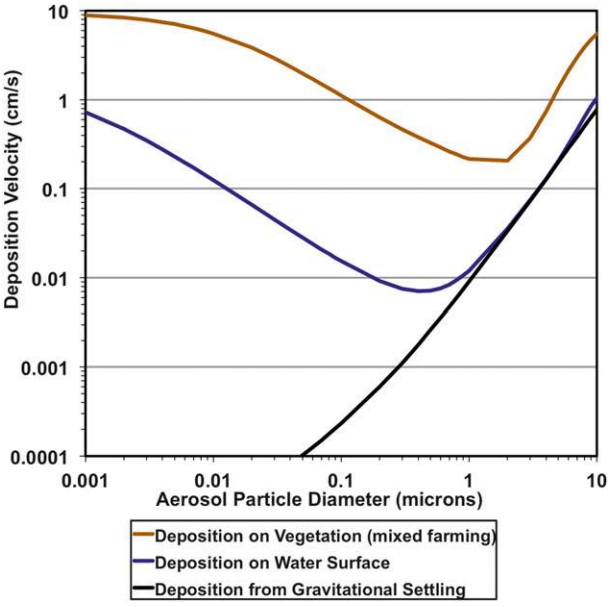

FIG. 8. Variations in aerosol dry deposition velocity (cm s^{-1}) as a function of aerosol size and surface or layer upon which deposition occurs.

h. *Aerosol direct radiation effects*

An aerosol radiative transfer scheme, implemented by Stokowski (2005) into RAMS 4.3, has been applied to the nine aerosol species in RAMS 6.0. This scheme runs interactively with the hydrometeor-sensitive two-stream radiation model of Harrington (1997) that computes the absorption and scattering of primary atmospheric gases (Ritter and Geleyn 1992) and hydrometeors (Mie 1908) across eight radiation bands. Mie theory is also applied to the aerosol distributions to compute their impact on the optical depth (τ_p, total extinguished radiation), the single-scatter albedo (ω_p, fraction of extinguished radiation that is scattered), and the asymmetry parameter (G_p, direction of scattered radiation). Mishchenko et al. (1997) concluded that the optical parameters differ very little between a spherical and nonspherical aerosol assumption. Under a spherical aerosol assumption, the Mie solution for aerosols only requires input of the wavelength of incident radiation, the wavelength-dependent complex index of refraction of the aerosol species (d'Almeida et al. 1991; Haywood et al. 2003, for mineral dust), and aerosol size. A Mie scattering solver, based on Bohren and Huffman (1983), was run offline to generate 4D lookup tables with values of the extinction coefficient (Q_{ext}), the scattering coefficient (Q_{scat}), and the asymmetry parameter (G_{asym}) for each of the radiation bands. The lookup tables vary with aerosol type (ammonium sulfate, sea salt, and mineral dust), radiation band (three solar, five near infrared), aerosol radius (17 radius bins from 15 nm up to 33.0 μm), and relative humidity (1% increments for the deliquescence growth factor from 80% to 100%).

At each model radiation time step, the aerosol *distribution-total* Mie coefficients are accessed from the lookup tables and optical parameters are computed for each aerosol species a by summing the size and number of concentration-weighted bin-resolved coefficients over the distributions in 17 (aerobins) size bins i (in mks units) as

$$\beta_{\text{ext},a} = \sum_{i=1}^{\text{aerobins}} \frac{\pi}{4} D_i N_i Q_{\text{ext},i},$$

$$\beta_{\text{scat},a} = \sum_{i=1}^{\text{aerobins}} \frac{\pi}{4} D_i N_i Q_{\text{scat},i}, \quad \text{and}$$

$$G_{\text{asym},a} = \sum_{i=1}^{\text{aerobins}} N_i G_i \tag{27}$$

and

$$\tau_a = \beta_{\text{ext},a} \Delta z,$$

$$\omega_a = \frac{\beta_{\text{scat},a}}{\beta_{\text{ext},a}}, \quad \text{and}$$

$$G_a = \frac{G_{\text{asym},a}}{N_t}. \tag{28}$$

The optical parameters for all aerosol species are combined similarly to hydrometeor extinction and scattering following Liou et al. (1978) and Slingo and Schrecker (1982):

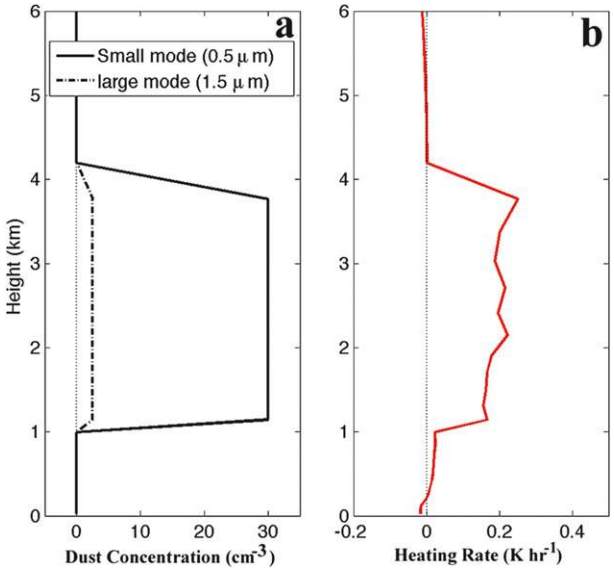

FIG. 9. Vertical profiles of (a) dust aerosol number concentration (cm^{-3}) and (b) the resulting heating rate ($K\,h^{-1}$) due to solar absorption at 1 h into an idealized, cloud-free simulation with incoming solar radiation of $\sim 1100\,W\,m^{-2}$. (Figure is courtesy of L. Grant.)

$$\tau_p = \sum_{a=1}^{\text{aerotypes}} \tau_a,$$

$$\omega_p = \frac{\sum_{a=1}^{\text{aerotypes}} \omega_a \tau_a}{\sum_{a=1}^{\text{aerotypes}} \tau_a}, \quad \text{and}$$

$$G_p = \frac{\sum_{a=1}^{\text{aerotypes}} G_a \omega_a \tau_a}{\sum_{a=1}^{\text{aerotypes}} \omega_a \tau_a}. \tag{29}$$

Summation of the absorption and scattering by aerosol particles, hydrometeors, and atmospheric gases across all radiation bands allows for computation of total atmospheric net radiation fluxes as well as heating rate profiles.

An idealized simulation was run to assess the aerosol radiation scheme in a controlled environment. Dust layer concentrations for the submicrometer and supermicrometer modes (Fig. 9a) were approximated from the vertical profiles of aerosols shown in DeMott et al. (2003). The previously used thermodynamic sounding was applied, though initial winds were set to zero to minimize short-term mixing of the aerosol layer. The solar angle was set at 65°, and incoming solar radiation at the top of the aerosol layer (4 km) is $\sim 1100\,W\,m^{-2}$. Figure 9b displays the radiative impact of dust particles in a noncloudy atmosphere after 1 h. The radiative impacts of dust lead to an increase in the heating rate in the dust layer of $\sim 0.2\,K\,h^{-1}$. This falls within the range of heating rates shown by Carlson and Benjamin (1980) when integrated over a full solar day.

3. Testing of new modules

Recent developments described herein have been tested in simulated cases of precipitating stratocumulus clouds, deep convection, and winter orographic precipitation. In these cases, we examined the aerosol sensitivity with regard to 1) aerosol solubility, 2) aerosol regeneration, 3) precipitation scavenging, 4) nucleation scavenging, and 5) the DeMott ice nucleation scheme.

The stratocumulus simulations (referred to as ATEX) were initialized horizontally homogeneous with a sounding from the Atlantic Trade Wind Experiment (ATEX) experiment (Stevens et al. 2001). Simulations were run in 2D for 24 h with periodic boundary conditions, 200-m horizontal grid spacing, 50-m vertical grid spacing, and an ocean surface with SST of 298 K. A sample cross section of the precipitating stratocumulus field is shown in Fig. 10a. Simulations of deep convection (referred to as STORM) were initialized horizontally homogeneous with a high CAPE sounding suitable for producing a supercell thunderstorm; this is the same set of initial conditions from Saleeby and Cotton (2004a). The storm was simulated for 2 h with 1-km horizontal grid spacing, 100-m vertical grid spacing at the surface stretched to 1000 m aloft, and convection was initiated with a 2-K warm bubble. A sample cross section through the developed supercell is shown in Fig. 10b. Last, we ran the winter orographic snowfall experiments (referred to as TOPO) for 42 h over the central mountains of Colorado for a snowfall event occurring 12–13 February 2010, following Saleeby et al. (2013). For these simulations, we initialized and boundary nudged with the Global Forecast System reanalysis, triple nested our model domain down to 3-km horizontal grid spacing, used 75-m vertical grid spacing at the surface stretched to 800 m aloft, and focused the fine mesh grid on the Park Range of Colorado. A cross section through a representative orographic cloud is displayed in Fig. 10c; cross-barrier flow is left to right. All simulations were run with the two-moment RAMS microphysics described herein.

For each simulation, aerosols were initialized with a vertically decreasing profile of ammonium sulfate aerosols with 0.04 micrometers median radius [similar to Saleeby et al. (2013)]. Initial maximum aerosol concentrations were $1000\,cm^{-3}$ for the ATEX and STORM simulations and $1500\,cm^{-3}$ for TOPO. The higher concentration for

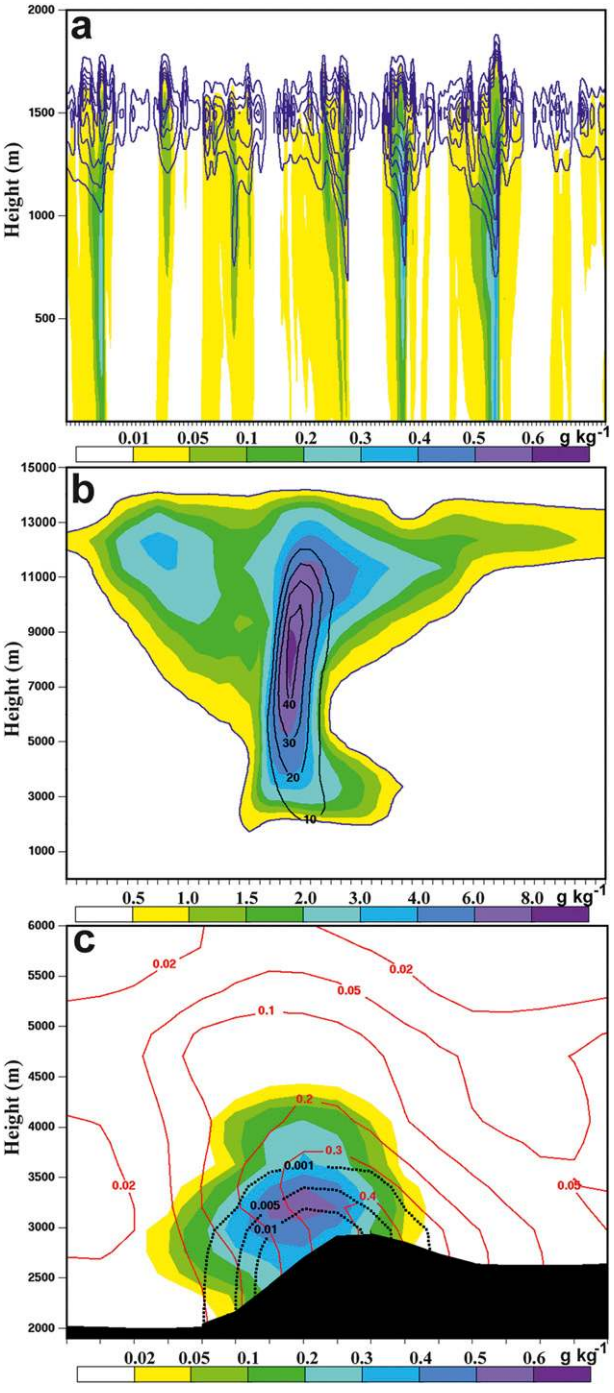

FIG. 10. Representative cross sections of the simulated (a) stratocumulus deck (rain mixing ratio is shaded and cloud mixing ratio is contoured with 0.1 contour interval), (b) supercell thunderstorm (condensate mixing ratio is shaded and positive vertical motion is contoured), and (c) winter orographic cloud (cloud water is shaded, snow is contoured red, and graupel is contoured black). Mixing ratios are in grams per kilogram, and vertical motion is in meters per second.

the TOPO simulations was set to that used in the simulations by Saleeby et al. (2013). For direct comparison between the Meyers and DeMott IN schemes, a common IN concentration profile was initialized that scales with the decrease in density with height with a maximum concentration of $10\,L^{-1}$. In the control simulations aerosols are 90% soluble, removed via nucleation and precipitation scavenging, and regenerated via hydrometeor evaporation. Heterogeneous ice nucleation is represented by the Meyers scheme.

For each event type (ATEX, STORM, and TOPO), five sensitivity tests were performed in which a single aerosol effect was modified relative to the control simulation: 1) aerosol solubility was reduced from 90% to 5%, 2) aerosol regeneration was turned off, 3) aerosol precipitation scavenging was turned off, 4) aerosol nucleation scavenging was turned off (aerosol nucleation was supersaturation limited such that droplet number concentration cannot exceed aerosol number concentration), and 5) the IN scheme was changed from Meyers to DeMott. For these five sensitivity experiments, we will focus the discussion on their impact on precipitation rates. Figure 11 reveals histograms of the spatial and temporal summation of the counts of grid cells that fall within bins of light, moderate, and heavy precipitation rate ($mm\,h^{-1}$). Note from the panel labels that cases vary by row and precipitation rate varies by column; further, the scales of gridcell count vary in each panel for visualization purposes. The percentage change relative to the control simulation is displayed above each sensitivity test histogram.

One of the most noticeable characteristics drawn from these histograms is that the various aerosol schemes are of differing importance among simulated cloud systems. In the ATEX simulations, both the low solubility and no-regeneration simulations lead to substantial percentage increases in all precipitate rate bins. Both of these experiments lead to production of fewer but larger nucleated cloud droplets, relative to the control, that produce an efficient warm rain process and greater precipitation production. In the test with no precipitation scavenging, more aerosols remain available for nucleation. This leads to more numerous cloud droplets and slight precipitation suppression, though the suppression is small. It should be noted that the median radius of the initial aerosol distribution is in the size range where precipitation scavenging is limited. Had we initialized with supermicrometer-sized aerosols or much smaller aerosols, this scavenging effect would likely have been larger, but the impact of solubility and nucleation scavenging would be substantially altered. In the test with no nucleation scavenging, there is a large increase in lightly precipitating grid cells and a decrease in heavy

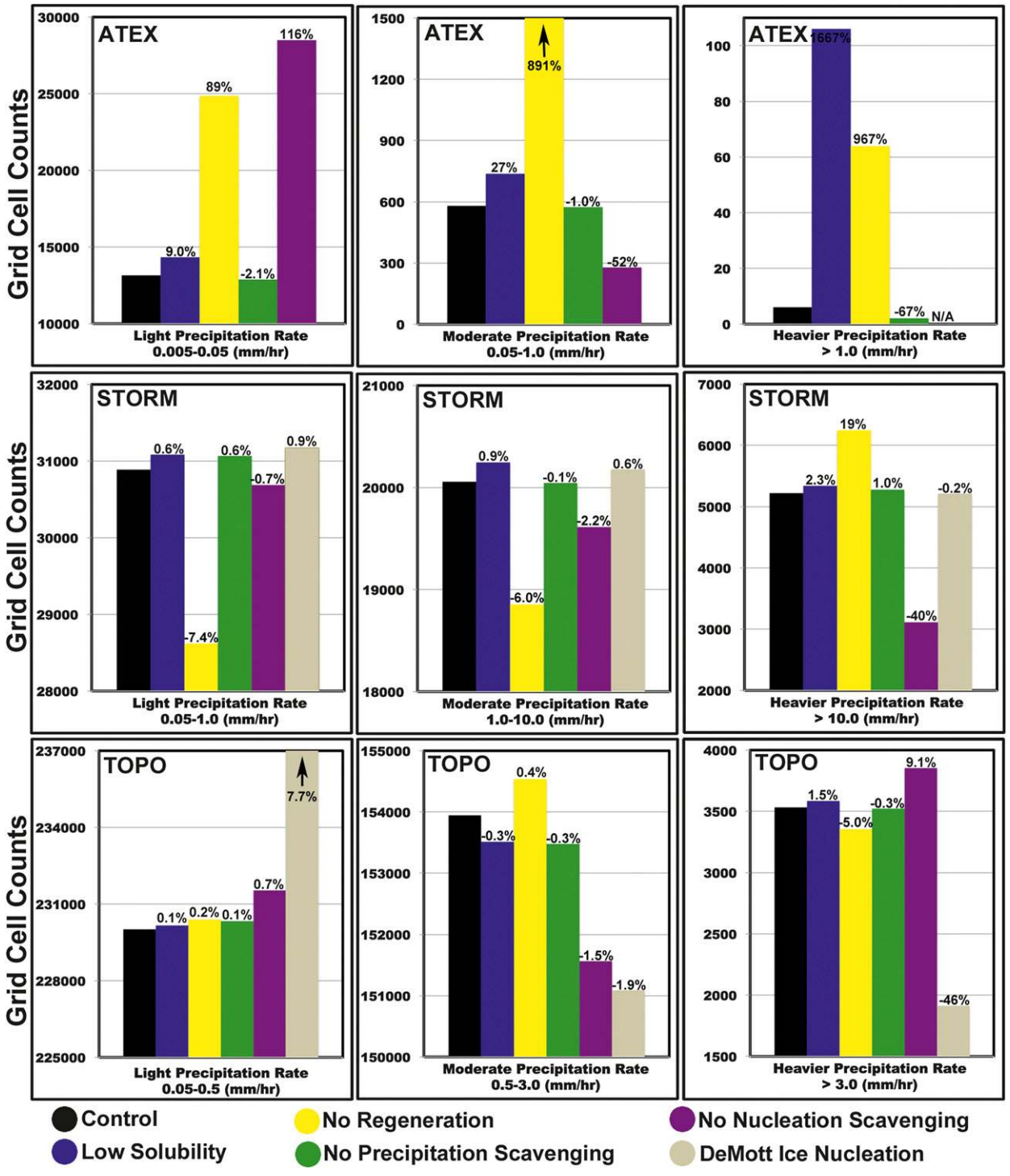

FIG. 11. Histograms of the gridcell counts of (left) light, (center) moderate, and (right) heavy precipitation rates (mm h^{-1}) summed over space and time for each of the sensitivity experiments from the (top) ATEX, (middle) STORM, and (bottom) TOPO simulations. For each of the sensitivity experiments, the percentage change relative to the control run is displayed above the corresponding histogram. Note that scales vary and the definitions of light, moderate, and heavy precipitation rate differ among cases.

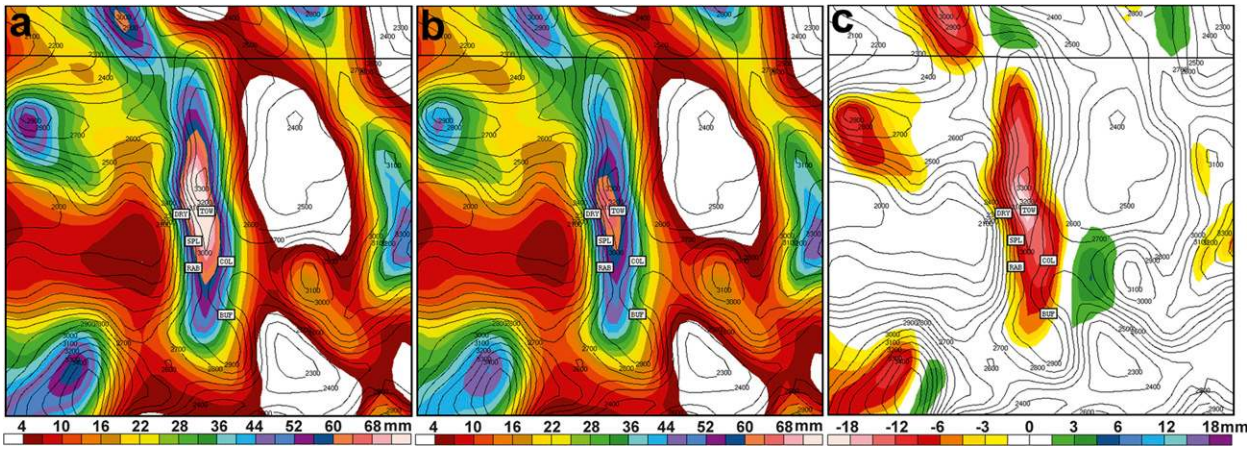

FIG. 12. Plan-view plots over the Park Range of total precipitation (colors; mm) with use of the heterogeneous ice nucleation scheme of (a) Meyers et al. (1992) and (b) DeMott et al. (2010). (c) The precipitation difference (mm) taken as DeMott–Meyers. Topography (m) is contoured in black. The location of Storm Peak Laboratory and SNOTEL sites are denoted on the figures as discussed in Saleeby et al. (2013).

precipitation. Without nucleation scavenging, the model tends to have higher cloud droplet concentration over a greater area, thus leading to suppression of heavier precipitation and an increase in the frequency of light precipitation. The DeMott IN scheme is not tested in the ATEX case since all clouds are below the freezing level.

In the STORM simulations, only the regeneration and nucleation scavenging tests produce precipitation rate changes greater than a few percent. Without aerosol regeneration, the environment remains cleaner and leads to a more efficient warm rain process. This results in fewer lightly and moderately precipitating grid cells and a greater number of heavily precipitating grid cells. Without nucleation scavenging, there is the potential for enhanced cloud droplet production, which leads to droplets of smaller size. This response leads to suppression of precipitation, with the greatest impact on heavy precipitation. The DeMott IN test shows very little change in this case since heterogeneous ice nucleation produces few ice crystals in comparison with homogeneous freezing of cloud droplets lofted above the −40°C level by the updraft. The impact of these aerosol parameterizations in the STORM case is small relative to the percentage impact in the ATEX case. The STORM case is strongly dynamically forced, thus making these particular aerosol parameterizations of secondary importance.

In the TOPO simulations, the model responds most noticeably to the choice of IN parameterization compared to the other aerosol tests. In a winter orographic precipitation environment, cloud nucleating aerosols primarily affect precipitation by modifying the riming efficiency of snow falling through clouds of supercooled water. This may have a substantial localized effect and potentially induce changes in the spatial distribution of precipitation (Saleeby et al. 2009, 2013). When switching from the Meyers to the DeMott IN scheme, there is a substantial decrease in heavy precipitation. Figure 12 displays plan views of the total accumulated precipitation across the domain as well as the difference in total precipitation. Along the ridgeline and windward slope of the Park Range in the center of the domain, the accumulated precipitation is reduced upward of 20%. A comparison between these tests and those from Saleeby et al. (2013) suggests that total precipitation resulting from the DeMott IN parameterization may fall more inline with Snowpack Telemetry (SNOTEL) observations within the region of maximum snowfall.

4. Summary and conclusions

Recent developments in the CSU-RAMS model, version 6.0, provide for a more comprehensive aerosol model that extends beyond the capabilities of previous aerosol–microphysics–related research (e.g., Saleeby et al. 2009, 2013; van den Heever et al. 2006, 2011). This work has sought to develop and describe a more unified version of the aerosol model embedded within RAMS and builds upon the prior work by various authors and colleagues. The aerosol model represents nine aerosol species: submicrometer and supermicrometer modes of ammonium sulfate, mineral dust, and regenerated aerosols and three modes of sea salt. Aerosol concentrations can be prescribed and/or the user can make use of the dust and sea salt source models for emissions of these species. Each of these aerosol species may

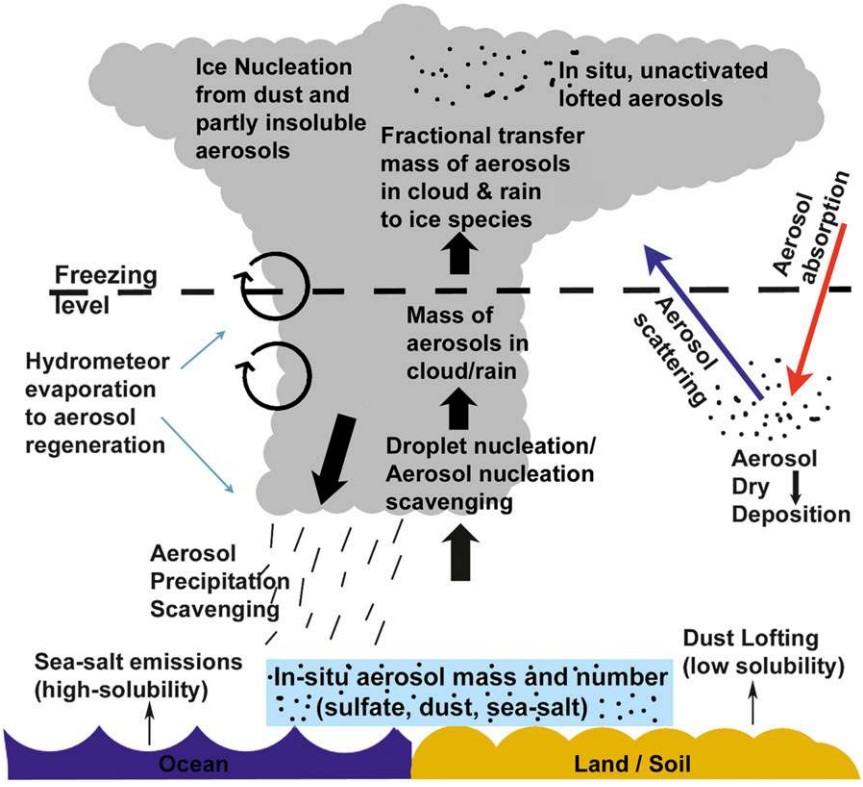

FIG. 13. Schematic depicting the aerosol-related sources, sinks, transfer mechanisms, and radiation effects that are represented in the CSU-RAMS aerosol module.

compete for activation and subsequent nucleation of new cloud droplets. All particles $>0.5\,\mu$m, except sea salt, may potentially act as heterogeneous IN. Further, each aerosol species may have a distinct solubility, contribute to the radiation budget, and undergo dry deposition (gravitational settling), wet deposition (precipitation scavenging) and evaporative regeneration. Figure 13 offers a schematic depicting the aerosol-related sources, sinks, transfer mechanisms, and radiation effects.

Sensitivity tests of the influence of aerosol solubility, nucleation scavenging, precipitation scavenging, and regeneration were performed for simulations of stratocumulus clouds, deep convection, and winter orographic precipitation. The Meyers and DeMott heterogeneous ice nucleation schemes were also compared. Results indicate that in cloud systems with active warm rain processes, the representations of aerosol nucleation scavenging and regeneration are most influential among these five tested aerosol parameterizations, though, in weakly forced clouds, aerosol solubility can be important. In deep convection, the dynamical influence overwhelms these secondary aerosol effects and the degree of impact is less than in shallow clouds. The impact of the DeMott ice nucleation scheme is limited in deep convection since other ice nucleation processes are dominant. However, in winter orographic precipitation, the DeMott scheme reduces orographic precipitation and appears to bring snowfall accumulations more in line with observations. In future work, we will continue to refine the treatment of aerosols and work to improve the simulation of their physical impacts on cloud and climate systems.

Acknowledgments. This work was supported by the National Science Foundation Division of Atmospheric Sciences Grants 1005316 and 1005020. We thank Robert B. Seigel for his work with the dust source model and Fig. 5 and Leah Grant for testing the aerosol radiation model and for Fig. 9. We also thank Dr. Paul DeMott for his insightful guidance in implementing the heterogeneous ice nucleation parameterization. (All three contributors are affiliated with the Department of Atmospheric Science at Colorado State University.)

REFERENCES

Albrecht, B., 1989: Aerosols, cloud microphysics, and fractional cloudiness. *Science,* **245,** 1227–1230.

Alfaro, S. C., and L. Gomes, 2001: Modeling mineral aerosol production by wind erosion: Emission intensities and aerosol size distributions in source areas. *J. Geophys. Res.,* **106,** 18 075–18 084.

Baron, P. A., and K. Willeke, 2001: *Aerosol Measurement: Principles, Techniques and Applications.* 2nd ed. Wiley-Interscience, 1131 pp.

Bernardet, L., and W. R. Cotton, 1998: Multiscale evolution of a derecho-producing mesoscale convective system. *Mon. Wea. Rev.,* **126,** 2991–3015.

Berthet, S., M. Leriche, J.-P. Pinty, J. Cuesta, and G. Pigeon, 2010: Scavenging of aerosol particles by rain in a cloud resolving model. *Atmos. Res.,* **96,** 325–336.

Bohren, C. F., and D. R. Huffman, 1983: *Absorption and Scattering of Light by Small Particles*. John Wiley and Sons, 530 pp.

Carlson, T. N., and S. G. Benjamin, 1980: Radiative heating rates for Saharan dust. *J. Atmos. Sci.,* **37,** 193–213.

Carrio, G. G., and W. R. Cotton, 2011: Investigations of aerosol impacts on hurricanes: Virtual seeding flights. *J. Atmos. Chem. Phys.,* **11,** 2557–2567.

Castro, C. L., R. A. Pielke, and J. O. Adegoke, 2007: Investigation of the summer climate of the contiguous United States and Mexico using the Regional Atmospheric Modeling System (RAMS). Part I: Model climatology (1950–2002). *J. Climate,* **20,** 3844–3865.

Cheng, W. Y. Y., G. G. Carrio, W. R. Cotton, and S. M. Saleeby, 2009: Influence of atmospheric aerosols on the development of precipitating trade wind cumuli in a large eddy simulation. *J. Geophys. Res.,* **114,** D08201, doi:10.1029/2008JD011011.

Cotton, W. R., and Coauthors, 2003: RAMS 2001: Current status and future directions. *Meteor. Atmos. Phys.,* **82,** 5–29.

d'Almeida, G. A., P. Koepke, and E. P. Shettle, 1991: *Atmospheric Aerosols: Global Climatology and Radiative Characteristics.* A. Deepak Publishing, 580 pp.

Darby, L. S., R. M. Banta, and R. A. Pielke, 2002: Comparisons between mesoscale model terrain sensitivity studies and Doppler lidar measurements of the sea breeze at Monterey Bay. *Mon. Wea. Rev.,* **130,** 2813–2838.

DeMott, P. J., M. P. Meyers, and W. R. Cotton, 1994: Parameterization and impact of ice initiation processes relevant to numerical model simulations of cirrus clouds. *J. Atmos. Sci.,* **51,** 77–90.

——, K. Sassen, M. R. Poellot, D. Baumgardner, D. C. Rogers, S. D. Brooks, A. J. Prenni, and S. M. Kreidenweis, 2003: African dust aerosols as atmospheric ice nuclei. *Geophys. Res. Lett.,* **30,** 1732, doi:10.1029/2003GL017410.

——, and Coauthors, 2010: Predicting global atmospheric ice nuclei distributions and their impacts on climate. *Proc. Natl. Acad. Sci. USA,* **107,** 11 217–11 222.

Ekman, A. M. L., C. Wang, J. Wilson, and J. Ström, 2004: Explicit simulations of aerosol physics in a cloud-resolving model: A sensitivity study based on an observed convective cloud. *Atmos. Chem. Phys.,* **4,** 773–791.

——, ——, J. Ström, and R. Krejci, 2006: Explicit simulation of aerosol physics in a cloud-resolving model: Aerosol transport and processing in the free troposphere. *J. Atmos. Sci.,* **63,** 682–696.

Engström, A., A. M. L. Ekman, R. Krejci, J. Ström, M. de Reus, and C. Wang, 2008: Observational and modeling evidence of tropical deep convective clouds as a source of mid-tropospheric accumulation model aerosols. *Geophys. Res. Lett.,* **35,** L23813, doi:10.1029/2008GL035817.

Fan, T., and O. B. Toon, 2011: Modeling sea-salt aerosol in a coupled climate and sectional microphysical model: Mass, optical depth and number concentration. *Atmos. Chem. Phys.,* **11,** 4587–4610.

Fécan, F., B. Marticorena, and G. Bergametti, 1999: Parameterization of the increase of the Aeolian erosion threshold wind friction velocity due to soil moisture for arid and semi-arid areas. *Ann. Geophys.,* **17,** 149–157.

Feingold, G., and A. J. Heymsfield, 1992: Parameterizations of condensational growth of droplets for use in general circulation models. *J. Atmos. Sci.,* **49,** 2325–2342.

Fitzgerald, J. W., 1975: Approximation formulas for the equilibrium size of an aerosol particle as a function of its dry size and composition and the ambient relative humidity. *J. Appl. Meteor.,* **14,** 1044–1049.

Flossmann, A. I., W. D. Hall, and H. R. Pruppacher, 1985: A theoretical study of the wet removal of atmospheric pollutants. Part I: The redistribution of aerosol particles captured through nucleation and impaction scavenging by growing cloud drops. *J. Atmos. Sci.,* **42,** 583–606.

——, H. R. Pruppacher, and J. H. Topalian, 1987: A theoretical study of the wet removal of atmospheric pollutants. Part II: The uptake and redistribution of $(NH_4)_2S0_4$ particles and SO_2 gas simultaneously scavenged by growing cloud drops. *J. Atmos. Sci.,* **44,** 2912–2923.

Fridlind, A. M., A. S. Ackerman, G. McFarquhar, G. Zhang, M. R. Poellot, P. J. DeMott, A. J. Prenni, and A. J. Heymsfield, 2007: Ice properties of single-layer stratocumulus during the Mixed-Phase Arctic Cloud Experiment: 2. Model results. *J. Geophys. Res.,* **112,** D24202, doi:10.1029/2007JD008646.

Ginoux, P., M. Chin, I. Tegen, J. M. Prospero, B. Holben, O. Dubovik, and S.-J. Lin, 2001: Sources and distributions of dust aerosols simulated with the GOCART model. *J. Geophys. Res.,* **106,** 20 255–20 273.

Harrington, J. Y., 1997: The effects of radiative and microphysical processes on simulated warm and transition season Arctic stratus. Ph.D. dissertation, Colorado State University, Atmospheric Science Paper 637, 289 pp.

Haywood, J., and Coauthors, 2003: Radiative properties and direct radiative effect of Sharan dust measured by the C-130 aircraft during SHADE: 1. Solar spectrum. *J. Geophys. Res.,* **108,** 8577, doi:10.1029/2002JD002687.

Hegg, D. A., S. A. Rutledge, and P. V. Hobbs, 1986: A numerical model for sulfur and nitrogen scavenging in narrow cold-frontal rainbands: 2. Discussion of chemical fields. *J. Geophys. Res.,* **91,** 14 403–14 416.

Heymsfield, A. J., and R. M. Sabin, 1989: Cirrus crystal nucleation by homogeneous freezing of solution droplets. *J. Atmos. Sci.,* **46,** 2252–2264.

Igel, A., S. C. van den Heever, C. Naud, S. M. Saleeby, and D. Posselt, 2013: Sensitivity of warm frontal processes to cloud-nucleating aerosol concentrations. *J. Atmos. Sci.,* **70,** 1768–1783.

Jiang, H., and G. Feingold, 2006: Effect of aerosol on warm convective clouds: Aerosol-cloud-surface flux feedbacks in a new coupled large eddy model. *J. Geophys. Res.,* **111,** D01202, doi:10.1029/2005JD006138.

——, ——, W. R. Cotton, and P. G. Duynkerke, 2001: Large-eddy simulations of entrainment of cloud condensation nuclei into the Arctic boundary layer: May 18, 1998, FIRE/SHEBA case study. *J. Geophys. Res.,* **106,** 15 113–15 122.

Kok, J. F., 2011: Does the size distribution of mineral dust aerosols depend on the wind speed at emission? *Atmos. Chem. Phys.,* **11,** 10 149–10 156.

Lee, S. S., 2012: Effect of aerosol on circulations and precipitation in deep convective clouds. *J. Atmos. Sci.,* **69,** 1957–1974.

——, J. E. Penner, and S. M. Saleeby, 2009: Aerosol effects on liquid-water path of thin stratocumulus clouds. *J. Geophys. Res.,* **114,** D07204, doi:10.1029/2008JD010513.

Liou, K. N., K. P. Freeman, and T. Sasamori, 1978: Cloud and aerosol effects on the solar heating rate of the atmosphere. *Tellus,* **30,** 62–70.

Lu, L., and W. J. Shuttleworth, 2002: Incorporating NDVI-derived LAI into the climate version of rams and its impact on regional climate. *J. Hydrometeor.,* **3,** 347–362.

Marticorena, B., and G. Bergametti, 1995: Modeling the atmospheric dust cycle: 1. Design of a soil-derived dust emission scheme. *J. Geophys. Res.,* **100,** 16 415–16 430.

Meyers, M. P., P. J. DeMott, and W. R. Cotton, 1992: New primary ice nucleation parameterizations in an explicit cloud model. *J. Appl. Meteor.,* **31,** 708–721.

——, R. L. Walko, J. Y. Harrington, and W. R. Cotton, 1997: New RAMS cloud microphysics parameterization. Part II. The two-moment scheme. *Atmos. Res.,* **45,** 3–39.

Mie, G., 1908: Beiträge zur Optik trüber Medien, spieziell kolloidaler Metallösungen (Contributions to the optics of turbid media, particularly of colloidal solutions). *Ann. Phys.,* **330,** 377–445, doi:10.1002/andp.19083300302.

Mishchenko, M. I., L. D. Travis, R. A. Kahn, and R. A. West, 1997: Modeling phase functions for dustlike tropospheric aerosols using a shape mixture of randomly oriented polydisperse spheroids. *J. Geophys. Res.,* **102,** 16 831–16 847.

O'Dowd, C. D., M. H. Smith, I. E. Consterdine, and J. A. Lowe, 1997: Marine aerosol, sea-salt, and the marine sulphur cycle: A short review. *Atmos. Environ.,* **31,** 73–80.

——, J. A. Lowe, and M. H. Smith, 1999: Coupling sea-salt and sulphate interactions and its impact on cloud droplet concentration predictions. *Geophys. Res. Lett.,* **26,** 1311–1314.

Olsson, P., and W. R. Cotton, 1997: Balanced and unbalanced circulations in a primitive equation simulation of a midlatitude MCC. Part I: The numerical simulation. *J. Atmos. Sci.,* **54,** 457–478.

Petters, M. D., and S. M. Kreidenweis, 2007: A single parameter representation of hygroscopic growth and cloud condensation nucleus activity. *Atmos. Chem. Phys.,* **7,** 1961–1971.

Pierre, C., G. Bergametti, B. Marticorena, E. Mougin, C. Bouet, and C. Schmechtig, 2012: Impact of vegetation and soil moisture seasonal dynamics on dust emissions over the Sahel. *J. Geophys. Res.,* **117,** D06114, doi:10.1029/2011JD016950.

Reutter, P., and Coauthors, 2009: Aerosol- and updraft-limited regimes of cloud droplet formation: Influence of particle number, size and hygroscopicity on the activation of cloud condensation nuclei (CCN). *Atmos. Chem. Phys.,* **9,** 7067–7080.

Ritter, B., and J.-F. Geleyn, 1992: A comprehensive radiation scheme for numerical weather prediction models with potential application in climate situations. *Mon. Wea. Rev.,* **120,** 303–325.

Rutledge, S. A., D. A. Hegg, and P. V. Hobbs, 1986: A numerical model for sulfur and nitrogen scavenging in narrow cold-frontal rainbands: 1. Model description and discussion of microphysical fields. *J. Geophys. Res.,* **91,** 14 386–14 402.

Saleeby, S. M., and W. R. Cotton, 2004a: A large droplet mode and prognostic number concentration of cloud droplets in the Colorado State University Regional Atmospheric Modeling System (RAMS). Part I: Module descriptions and supercell test simulations. *J. Appl. Meteor.,* **43,** 182–195.

——, and ——, 2004b: Simulations of the North American monsoon system. Part I: Model analysis of the 1993 monsoon season. *J. Climate,* **17,** 1997–2018.

——, and ——, 2008: A binned approach to cloud-droplet riming implemented in a bulk microphysics model. *J. Appl. Meteor. Climatol.,* **47,** 694–703.

——, ——, D. Lowenthal, R. D. Borys, and M. A. Wetzel, 2009: Influence of cloud condensation nuclei on orographic snowfall. *J. Appl. Meteor. Climatol.,* **48,** 903–922.

——, ——, and J. Fuller, 2011: The cumulative impact of cloud droplet nucleating aerosols on orographic snowfall in Colorado. *J. Appl. Meteor. Climatol.,* **50,** 604–625.

——, ——, D. Lowenthal, and J. Messina, 2013: Aerosol impacts on the microphysical growth processes of orographic snowfall. *J. Appl. Meteor. Climatol.,* **52,** 834–852.

Seigel, R. B., and S. C. van den Heever, 2012: Mineral dust pathways into supercell storms. *J. Atmos. Sci.,* **69,** 1453–1473.

Seinfeld, J. H., and S. N. Pandis, 2006: *Atmospheric Chemistry and Physics: From Air Pollution to Climate Change.* John Wiley and Sons, 1203 pp.

Shao, Y., 2001: A model for mineral dust emission. *J. Geophys. Res.,* **106,** 20 239–20 254.

Slingo, A., and H. M. Schrecker, 1982: On the shortwave radiative properties of stratiform water clouds. *Quart. J. Roy. Meteor. Soc.,* **108,** 407–426.

Slinn, S. A., and W. G. N. Slinn, 1980: Predictions for particle deposition on natural waters. *Atmos. Environ.,* **14,** 1013–1026.

Slinn, W. G. N., 1982: Predictions for particle deposition to vegetative canopies. *Atmos. Environ.,* **16,** 1785–1794.

——, 1983: Precipitation scavenging. *Atmospheric Sciences and Power Production,* U.S. Department of Energy, 466–532.

Smith, M. A., 2007: Evaluation of mesoscale simulations of dust sources, sinks, and transport over the Middle East. M.S. thesis, Dept. of Atmospheric Science, Colorado State University, 126 pp.

Smith, M. H., M. P. Park, and I. E. Consterdine, 1993: Marine aerosol concentrations and estimated fluxes over the sea. *Quart. J. Roy. Meteor. Soc.,* **119,** 809–824.

Solomon, S., D. Qin, M. Manning, Z. Chen, M. Marquis, K. Averyt, M. Tignor, and H. L. Miller Jr., Eds., 2007: *Climate Change 2007: The Physical Science Basis.* Cambridge University Press, 996 pp.

Stevens, B., and Coauthors, 2001: Simulations of trade wind cumuli under a strong inversion. *J. Atmos. Sci.,* **58,** 1870–1890.

Stokowski, D., 2005: The addition of the direct radiative effect of atmospheric aerosols into the Regional Atmospheric Modeling System (RAMS). M.S. thesis, Dept. of Atmospheric Science, Colorado State University, Atmospheric Science Paper 637, 89 pp.

Storer, R. L., and S. C. van den Heever, 2013: Microphysical processes evident in aerosol forcing of tropical deep convective clouds. *J. Atmos. Sci.,* **70,** 430–446.

Tegen, I., and I. Fung, 1994: Modeling of mineral dust in the atmosphere: Sources, transport and optical thickness. *J. Geophys. Res.,* **99,** 22 897–22 914.

——, and A. A. Lacis, 1996: Modeling of particle size distribution and its influence on the radiative properties of mineral dust aerosol. *J. Geophys. Res.,* **101,** 19 237–19 244.

Twomey, S., 1974: Pollution and the planetary albedo. *Atmos. Environ.,* **8,** 1251–1256.

van den Heever, S. C., and W. R. Cotton, 2004: The impact of hail size on simulated supercell storms. *J. Atmos. Sci.,* **61,** 1596–1609.

——, G. G. Carrio, W. R. Cotton, P. J. DeMott, and A. J. Prenni, 2006: Impacts of nucleating aerosol on Florida storms. Part I: Mesoscale simulations. *J. Atmos. Sci.,* **63,** 1752–1775.

——, G. L. Stephens, and N. B. Wood, 2011: Aerosol indirect effects on tropical convection characteristics under conditions of radiative-convective equilibrium. *J. Atmos. Sci.,* **68,** 699–718.

Verlinde, J., P. J. Flatau, and W. R. Cotton, 1990: Analytical solutions to the collection growth equation: Comparison with approximate methods and application to cloud microphysics parameterization schemes. *J. Atmos. Sci.,* **47,** 2871–2880.

Walko, R. L., W. R. Cotton, M. P. Meyers, and J. Y. Harrington, 1995: New RAMS cloud microphysics parameterization: Part I. The single-moment scheme. *Atmos. Res.,* **38,** 29–62.

——, ——, ——, and ——, 2000a: Efficient computation of vapor and heat diffusion between hydrometeors in a numerical model. *Atmos. Res.,* **53,** 171–183.

——, and Coauthors, 2000b: Coupled atmosphere–biophysics–hydrology models for environmental modeling. *J. Appl. Meteor.,* **39,** 931–944.

Wang, C., and J. S. Chang, 1993: A three-dimensional numerical model of cloud dynamics, microphysics, and chemistry: 1. Concepts and formulation. *J. Geophys. Res.,* **98,** 14 827–14 844.

Wang, X., L. Zhang, and M. D. Moran, 2010: Uncertainty assessment of current size-resolved parameterizations for below-cloud particle scavenging by rain. *Atmos. Chem. Phys. Discuss.,* **10,** 2503–2548.

Ward, D. S., T. Eidhammer, W. R. Cotton, and S. M. Kreidenweis, 2010: The role of the particle size distribution in assessing aerosol composition effects on simulated droplet activation. *Atmos. Chem. Phys.,* **10,** 5435–5447.

Zhang, H., G. M. McFarquhar, S. M. Saleeby, and W. R. Cotton, 2007: Impacts of Saharan dust as CCN on the evolution of an idealized tropical cyclone. *Geophys. Res. Lett.,* **34,** L14812, doi:10.1029/2007GL029876.

Zhang, L., S. Gong, J. Padro, and L. Barrie, 2000: A size-segregated particle dry deposition scheme for an atmospheric aerosol module. *Atmos. Environ.,* **35,** 549–560.